Materials Science & Engineering C 123 (2021) 112004

Contents lists available at ScienceDirect

Materials Science & Engineering C

journal homepage: www.elsevier.com/locate/msec

Effective antimicrobial activity of ZnO and Yb-doped ZnO nanoparticles against *Staphylococcus aureus* and *Escherichia coli*

Diego Eloyr Navarro-López [a], Rebeca Garcia-Varela [a], O. Ceballos-Sanchez [b,*], A. Sanchez-Martinez [c], Gildardo Sanchez-Ante [d], Kaled Corona-Romero [a], D. A. Buentello-Montoya [a], Alex Elías-Zuñiga [e], Edgar R. López-Mena [a,*]

[a] Tecnologico de Monterrey, Campus Guadalajara, Av. Gral Ramón Corona No 2514, Colonia Nuevo México, 45201 Zapopan, Jal, Mexico
[b] Departamento de Ingeniería de Proyectos, CUCEI, Universidad de Guadalajara, Av. José Guadalupe Zuno # 48, Industrial los Belenes, Zapopan, Jalisco 45157, Mexico
[c] CONACYT-Unidad Académica de Ciencias Químicas, Universidad Autónoma de Zacatecas, Campus Siglo XXI, Carretera Zacatecas - Guadalajara Km 6, Ejido La Escondida, 98160, Zacatecas, Zacatecas, Mexico
[d] Universidad Politecnica de Yucatan, Carretera Merida-Tetiz, Km. 4.5, Ucu, YUC 97357, Mexico
[e] Tecnologico de Monterrey, Escuela de Ingeniería y Ciencias, Campus Monterrey, Monterrey, Nuevo León 64849, Mexico

ARTICLE INFO

Keywords:
Rare-earth doped
Ytterbium
ZnO nanoparticles
Antimicrobial activity

ABSTRACT

Nanostructured $Zn_{1-x}Yb_xO$ ($0.0 \leq x \leq 0.1$) powders were prepared by the solution method using polyvinyl alcohol (PVA) and sucrose. The effect of the ytterbium doping content on the structural, morphological, optical and antimicrobial properties was analyzed. X-ray diffraction (XRD) analysis revealed that the hexagonal wurtzite structure was retained, and no secondary phases due to doping were observed. The crystallite size was under 20 nm for all the $Zn_{1-x}Yb_xO$ ($0.0 \leq x \leq 0.1$) powders. The optical band gap was calculated, and the results revealed that this value increased with the ytterbium content, and the E_g values varied from 3.06 to 3.10 eV. The surface chemistry of the powders was analyzed using X-ray photoelectron spectroscopy (XPS), and the results confirmed the oxidation state of ytterbium as 3+ for all the samples. $Zn_{1-x}Yb_xO$ ($0.0 \leq x \leq 0.1$) nanoparticles were tested as antimicrobial agents against *Staphylococcus aureus* and *Escherichia coli*, resulting in a potential antimicrobial effect at most of the tested concentrations. These results were used in an artificial neural network (ANN). The results showed that it is possible to generate a model capable of forecasting the absorbance with good precision (error of 1–2%).

1. Introduction

In recent years, some multidrug-resistant (MDR) microorganisms have attracted attention in the nanotechnology field to study, assess and develop new elimination strategies [1,2]. Different nanomaterials, such as TiO_2, MgO, Ag_2O and ZnO, have been studied as potential antibacterial agents [3–5]. However, ZnO is the most promising due to its biocompatibility and low cost; previous reports have shown its bioactivity against *Staphylococcus aureus* and *Escherichia coli* [6]. These bacteria are of great importance in human health. *E. coli* is the most studied and extensively used prokaryotic organism; it is found virtually everywhere and is extremely common in human and some animal guts, and it has been linked to food-borne illnesses and outbreaks [7,8]. Additionally, *S. aureus,* which is widely found in humans as both a commensal and pathogenic bacterium [9], is the leading cause of bacteria-related heart diseases such as endocarditis, and other severe conditions such as osteoarticular, skin, soft tissue, and lung infections and infections due to contaminated medical devices [10].

Rare earth-doped nanomaterials, especially ZnO nanoparticles, have shown interesting and improved physical and chemical properties. La-, Ce-, Dy-, and Gd-doped ZnO nanoparticles have been used as antimicrobial agents against *Pseudomonas aeruginosa, S. aureus,* and *Salmonella paratyphi-B*, among others [11–13]. In these works, the increase in antibacterial activity was explained in terms of crystallite size and oxygen vacancies. The authors reported that when ZnO was doped, the crystallite size decreased, and the specific surface area increased. Additionally, rare earth ions can be introduced in the ZnO lattice as substitution ions, allowing the formation of oxygen vacancies. According to several reports, these are key factors that explain antimicrobial activity [14,15]. These characteristics are direct consequences of the

* Corresponding authors.
E-mail addresses: Ceballos0516@gmail.com (O. Ceballos-Sanchez), Edgarl@tec.mx (E.R. López-Mena).

https://doi.org/10.1016/j.msec.2021.112004
Received 27 December 2020; Received in revised form 14 February 2021; Accepted 20 February 2021
Available online 2 March 2021

synthesis method used to prepare the nanoparticles.

ZnO nanoparticles have been prepared following a wide variety of synthesis methods. Recently, *Echinochloa frumentacea* grain powder extract was used to prepare ZnO nanoparticles annealed at 600 °C for 4 h in an air atmosphere, resulting in particles with an average crystallite size of 35–45 nm [16]. The ZnO nanoparticles obtained by the microwave-assisted method at 500 °C exhibited a crystallite size of approximately 30 nm [17]. A precursor powder from Pechini's method was calcined at 450 °C for 3 h to obtain 40 nm ZnO nanoparticles [18]. Additionally, a coprecipitation method was used to prepare ZnO nanoparticles calcined at 450 °C for 3 h, resulting in an average crystallite size of 20 nm [19]. Additionally, the polymerization-solution method has been used to synthesize nanoparticles [20–22]. In this method, a polymer is used as a stabilizer agent, and sucrose is used as a chelating agent. During the synthesis process, a highly exothermic reaction occurs between the oxidant (metal nitrates) and the organic-fuel reductant (sucrose) in the presence of PVA, allowing metal oxide formation [23]. The heat necessary to allow and maintain the exothermic reaction is produced by chemical reagents, and an external source is required [24].

The objective of this work is to study the antimicrobial activity of $Zn_{1-x}Yb_xO$ (0, 1, 5, 10 at.%) nanoparticles against *Staphylococcus aureus* and *Escherichia coli*. The effect of the ytterbium content on structural parameters and stress was analyzed by X-ray diffraction (XRD) and the Williamson-Hall method. The role of the chemical agents used in the synthesis route was studied by Fourier transform infrared spectroscopy. The effect of the synthesis route on the morphological properties was observed by field emission scanning electron microscopy and high-resolution transmission electron microscopy. The specific surface area was obtained by the Brunauer–Emmett–Teller method. Optical analysis was carried out using UV spectroscopy. X-ray photoelectron spectroscopy was used for compositional analysis. Finally, the results of the antimicrobial activity tests when using nanoparticles were used to build an artificial neural network that can be used to plan future experiments.

2. Methods

2.1. Nanoparticle synthesis

In this work, $Zn_{1-x}Yb_xO$ (0, 1, 5, 10 at.%) nanoparticles were synthesized by a solution-polymerization method. All the chemicals were purchased form Sigma-Aldrich. For the method, two starter solutions were prepared. First, a solution with a 1:1 M ratio of PVA:sucrose (PVA a.m.w.: 70000–1000) was dissolved in 50 ml of deionized water with stirring at 50 °C (to dissolve PVA). At the same time, stoichiometric amounts of $Zn(NO_3)_26H_20$ (98%) and $Yb(NO_3)_35H_2O$ (99%) were dissolved in 50 ml of deionized water to obtain $Zn_{1-x}Yb_xO$ precursor solutions. After 1 h, the solutions were mixed and the pH was adjusted to 1.0 by adding citric acid (99.5%). Subsequently, the solutions were stirred at 80 °C until complete water evaporation. After that, the precursor powders obtained were dried at 200 °C for 4 h. Finally, the powders were calcined at 450 °C for 3 h in an air atmosphere.

2.2. Nanoparticle characterization techniques

The crystal structure of the $Zn_{1-x}Yb_xO$ (0, 1, 5, 10 at.%) powders was characterized by XRD using an Empyrean diffractometer (PANalyticalla) with a *Cu* anode ($\lambda = 1.5406$ Å). XRD patterns were obtained from a 20° to 80° (2θ) with a 0.01° step size. Attenuated total reflection Fourier transform infrared (ATR-FTIR) spectroscopy was employed to assess the presence of organic matter in the ZnO structure. ATR-FTIR spectra were recorded in the 4000–700 cm^{-1} range using a Nicolet iS50 FTIR (Thermo Scientific) spectrometer. The morphology of the Yb-doped ZnO thin films was investigated using FESEM (TESCAN MIRA3 model). The TEM/HRTEM/STEM analyses were carried out using aberration-corrected STEM with a Jeol ARM200F (200 kV) FEG-TEM/STEM microscope equipped with a CEOS Cs-corrector on the illumination system. High-angle annular dark field scanning transmission electron microscopy (HAADF-STEM) images were obtained by aberration-corrected STEM. The specific surface area (SBET) was determined using the BET method in a Bel-Japan Minisorp II instrument. Optical properties were investigated through absorption spectra were obtained using a Cary-300 UV–vis (Agilent Technologies) spectrometer equipped with a polytetrafluoroethylene (PTFE) integration sphere. XPS (Thermo Scientific, K-Alpha) was performed using a monochromatic Al K_α source (hv = 1486 eV) to determine the bonding states of Zn1-xYbxO (0, 1, 5, 10 at. %). All spectra were aligned to the C 1s signal located at 284.8 eV, which is associated mainly with adventitious carbon. The Zn 2*p*, O 1*s*, and Yb 4*d* core levels were determined at 90° and a pass energy of 15 eV.

2.3. Effect of nanoparticles on bacterial growth

S. aureus and *E. coli* inocula were prepared in a nutrient broth medium (Merck, Millipore), and the cultures were then incubated overnight at 30 °C. From the initial fresh culture, a series of dilutions (up to 10^{-6}) were prepared; 5 μl of each dilution was used to inoculate petri dishes containing agar and nanoparticles, which were incubated at 30 °C for 24 h; afterwards, observations were performed by means of a photodocumenter (UVP GelSolo, Analytikjena). To improve the nanoparticle dispersion, plates were prepared by placing a thin layer of culture on a solid culture medium (nutrient agar) composed of nutrient broth supplemented with 7.5 g/L agar and 0.4, 0.8 or 1 mg/mL of previously homogenized nanoparticles.

2.4. Quantitative determination of the effect of nanoparticles on bacterial growth

Quantitative determination of the effect of nanoparticles on bacterial growth was determined by monitoring the growth kinetics in a microplate spectrophotometer (Varioskan Lux, Thermo Scientific). To this end, overnight *S. aureus* (ATCC® 33594) and *E. coli* (ATCC® BAA-1025) cultures were prepared. Tubes containing culture medium were prepared and supplemented with 0.4, 0.8 and 1 mg/mL solutions of the different nanoparticles. Assays were performed in triplicate, and the initial OD600 was adjusted to approximately 0.1. Measurements were normalized by placing only the cultures prepared with nanoparticles, and a kinetic analysis was carried out by monitoring at 0, 2, 4, 6, 8, 10 and 24 h after inoculation.

3. Results and discussion

3.1. Powder XRD analysis

The XRD patterns of the $Zn_{1-x}Yb_xO$ (0, 1, 5, 10 at.%) powders after calcination in an air atmosphere at 450 °C for 3 h are shown in Fig. 1. All the peaks in the XRD pattern match JCPDS card number JCPDS 36–1451 of bulk ZnO, with lattice parameters of $a = b = 3.249$ Å and $c = 5.206$ Å and space group $P6_3mc$. The reflection peaks observed for the (100), (002), (101), (102), (110), (103), (200), (112) and (201) planes correspond to a hexagonal wurtzite structure. For $Zn_{1-x}Yb_xO$ (1, 5, 10 at.%) powders, no secondary peaks were observed, indicating that the ytterbium content (at.%) is less than the solubility limits. The XRD results show that all the powders obtained are polycrystalline. All the XRD patterns were plotted at the same scale to compare effects.

To understand the effect of the ytterbium content in the preferred orientation along the diffraction plane, the texture coefficient (TC) was calculated. Using XRD data, the values of $TC_{(hkl)}$ were obtained by Harrys texture analysis [25]:

$$TC_{(hkl)} = \frac{I(hkl)/I_0(hkl)}{N^{-1}\sum I(hkl)/I_0(hkl)} \quad (1)$$

where *I(hkl)* is the XRD intensity of the nanoparticles obtained by the

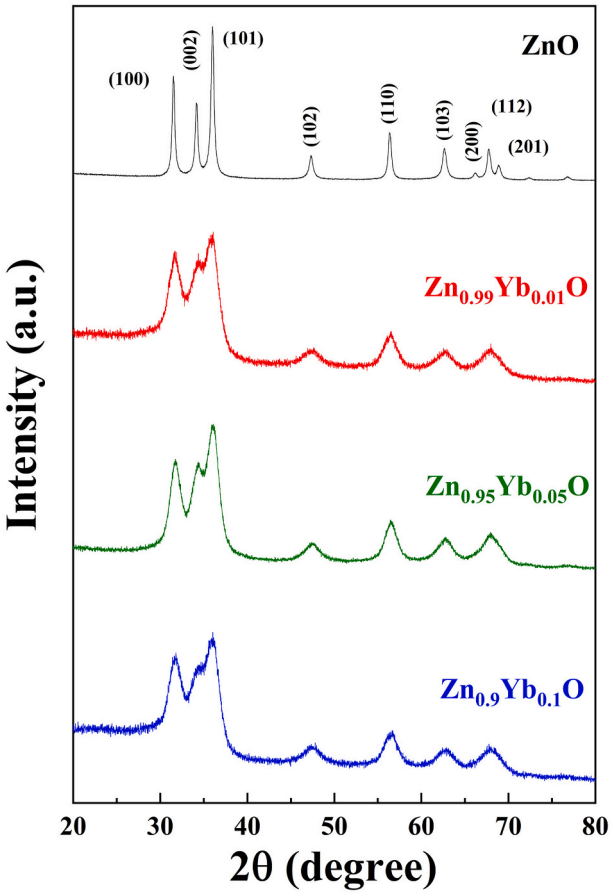

Fig. 1. XRD patterns of $Zn_{1-x}Yb_xO$ (0, 1, 5, 10 at.%) powders annealed at 450 °C for 3 h, prepared by the solution-polymerization method.

solution-polymerization method, $I_0(hkl)$ is the intensity of the standard pattern JCPDS 36–1451 and N is the number of diffraction peaks considered. If $TC_{(hkl)} = 1$, the sample exhibits randomly oriented crystallites, and if $TC_{(hkl)} > 1$, then the particles have grown with a certain preferred orientation. The TCs of $Zn_{1-x}Yb_xO$ (0, 1, 5, 10 at.%) are shown in Fig. 2. These analyses showed that all the undoped and doped ZnO particles exhibited the same behavior, which indicated a (100) preferred orientation. According to the TC values of the ZnO particles, randomly oriented crystallites were observed. The TC values for the (100) direction in $Zn_{1-x}Yb_xO$ (0, 1, 5, 10 at.%) powders varied from 1.3 to 1.7, while these values for (101) remained almost constant. The TC values for the (002) direction decreased from 1.17 to 0.51 as the ytterbium content increased. As stated in previous reports, increasing the doping level prevents grain growth in the (002) direction [26,27]. The dopant creates new nucleation centers, and as a result, the nucleation type changes from homogeneous to heterogeneous, which allows changes in the crystal structure [28,29].

The lattice parameters for $Zn_{1-x}Yb_xO$ (0, 1, 5, 10 at.%) powders were calculated from the (100) and (002) interplanar distances (d) using the following equation for the hexagonal crystal structure [30]:

$$\left(\frac{1}{d_{hkl}}\right)^2 = \frac{4}{3}\left(\frac{h^2 + k^2 + hk}{a^2}\right) + \left(\frac{l^2}{c^2}\right) \quad (2)$$

The 2(θ) positions of (100) and (002) and the interplanar distance are summarized in Table 1. These results demonstrate that the diffraction peaks of the doped samples have shifted toward higher angles when compared with those of the undoped samples. This shift is due to the differences in the ionic radii of Zn^{2+} (0.74 nm) and Yb^{3+} (0.868 nm). This effect can be attributed to substitutions in the tetrahedral sites of

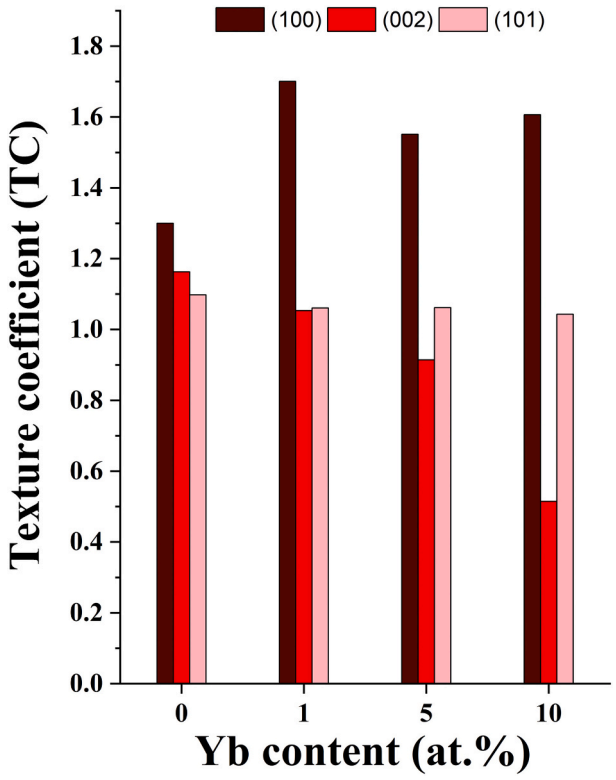

Fig. 2. Histogram representing the TC of the (100), (002) and (101) planes of $Zn_{1-x}Yb_xO$ (0, 1, 5, 10 at.%) powders.

Table 1
2(θ) position, interplanar distances (d) extracted from XRD analysis for $Zn_{1-x}Yb_xO$ (0, 1, 5, 10 at.%) powders.

Sample (at.%)	2θ (°) position		Interplanar distance (d_{hkl}) (Å) ±5%	
	(100)	(200)	d_{100}	d_{200}
ZnO	31.540	34.153	2.835	2.624
ZnO:Yb 1	31.668	34.382	2.822	2.606
ZnO:Yb 5	31.744	34.357	2.817	2.608
ZnO:Yb 10	31.783	34.487	2.813	2.598

Zn^{2+} in the ZnO matrix by Yb^{3+}, which allows lattice parameter distortion and stress development. Similar results have been reported when ZnO was doped with rare earth elements [31,32]. The calculated lattice parameters are given in Fig. 3a. The values of the a and c lattice parameters decreased as the ytterbium content increased. A similar behavior has been reported recently and is caused by two principal phenomena: the compressive hydrostatic pressure produced by rare earth dopants on the ZnO surface and the ytterbium atoms trapped in the nonequilibrium position, which are shifted toward an equilibrium position [33].

The effect of ytterbium content (at.%) on the average crystallite size (D) was calculated using the Scherrer equation [34]:

$$D = \frac{0.9\lambda}{\beta cos(\theta)} \quad (3)$$

where λ is the wavelength of the X-ray (1.5406 Å), θ the diffraction angle and β is the FWHM of the (101) plane of the XRD data. The 2(θ) and FWHM values used for this purpose are shown in Fig. 3b. The obtained values were 20.5 10.1, 10.0 and 11.0 nm (±5%) for $Zn_{1-x}Yb_xO$ (0, 1, 5, 10 at.%), respectively. The reduction in average crystallite size for Yb-doped ZnO nanoparticles can be associated with the distortion lattice in ZnO as ytterbium is incorporated, which decreases the rate of growth

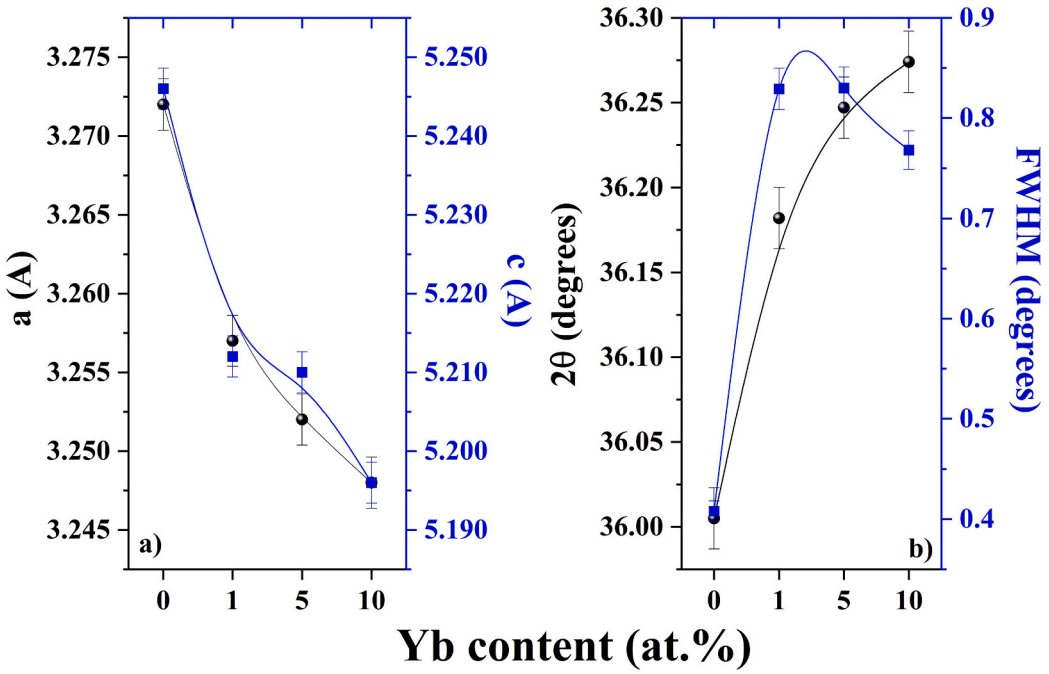

Fig. 3. Effects of ytterbium content on the a) lattice parameters *a* and *c*, b) shift of the (101) peak diffraction position and FWHM (degrees) in $Zn_{1-x}Yb_xO$ (0, 1, 5, 10 at.%) powders.

of ZnO particles [35]. Additionally, Fig. 3b shows a shift in the peak position of the (101) plane, which provides more evidence of ytterbium incorporation into ZnO. Furthermore, the incorporation of ytterbium decreased the crystallinity of the ZnO nanoparticles in conjunction with the increase in the FWHM values (Fig. 3b), consistent with the XRD results.

Previous results indicate a change in crystallite size and broadening of the XRD peaks; together, these factors together strain. The strain was analyzed by the Williamson-Hall method using the following formula [36]:

$$\beta cos(\theta) = \frac{\lambda K}{D} + 4\varepsilon sin(\theta) \quad (4)$$

where β is the FWHM of the diffraction peak, θ is the diffraction angle, λ is the wavelength of the X-ray (λ = 1.5406 Å), $K = 0.9$ is the geometric factor, D is the crystallite size and ε is the effective strain. This equation

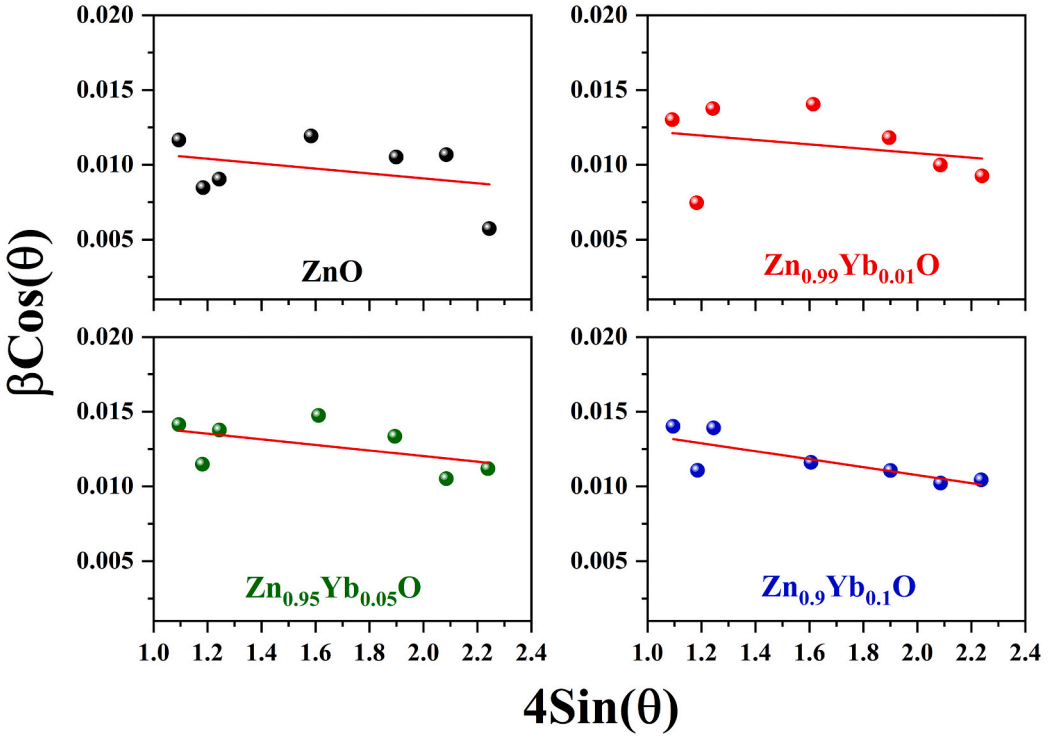

Fig. 4. W—H analysis of $Zn_{1-x}Yb_xO$ (0, 1, 5, 10 at.%) nanoparticles calcined at 450 °C assuming UDM.

represents the uniform deformation model (UDM); to use this model, it must be assumed that the strain is uniform in all crystallographic directions. Fig. 4 shows the W—H analysis for $Zn_{1-x}Yb_xO$ (0, 1, 5, 10 at.%) nanoparticles. From the linear fit, the strain was obtained from the slope, and the crystallite size determined the y-intercept of the linear fit. The values obtained for -ε were 0.11, 0.14, 0.19 and 0.27 for $Zn_{1-x}Yb_xO$ (0, 1, 5, 10 at.%), respectively. The negative strain is related to compressive strain, which is related to the lattice shrinkage observed. Similar W—H analysis behavior was reported when ZnO nanoparticles were doped with praseodymium and the doping concentration varied from 0 to 0.02 (wt%) [37]. As the ytterbium content increased, ε also increased because of lattice defects [38]. The crystallite sizes were also calculated, and the values were 11.21, 10.14, 8.78 and 8.61 (±5%) for $Zn_{1-x}Yb_xO$ (0, 1, 5, 10 at.%), respectively. These values are similar to those obtained by the Scherrer equation. However, the W—H analysis could be more accurate, as this study considers the effect of the crystallite size and strain simultaneously.

In addition, another structural parameter was investigated to understand the ytterbium effect on ZnO nanoparticles and corroborate the W—H analysis. From the lattice parameters (*a* and *c*), it was possible to calculate the variation in the Zn—O bond length, the degree of distortion and the unit cell volume using the following equations [39]:

$$L = \sqrt{\frac{a^2}{3} + (0.5 - d)^2 c^2} \tag{5}$$

$$R = \frac{2a(2/3)^{1/2}}{c} \tag{6}$$

$$V = \frac{\sqrt{3}a^2 c}{2} \tag{7}$$

where $d = a^2/3c^2 + 1/4$ (positional parameter). The packing factors (c/a) correspond to the ideal stoichiometric wurtzite structure (1.6333). The degree of distortion (*R*, $R = 1$ represents no distortion) varies from 1, which indicates the presence of oxygen and/or zinc vacancies [40]. The results are shown in Table 2. The Zn—O bond length decreased as the ytterbium content increased, resulting in strain. As a consequence of the decrease in the lattice parameter, the unit cell volume diminished. The *R* values obtained in all the samples indicate the presence of oxygen and/or zinc vacancies. The maximum c/a value corresponds to the $Zn_{0.95}Yb_{0.05}O$ sample.

3.2. Reaction mechanism and Fourier transform infrared (FTIR) spectral analysis

The reaction mechanism during the synthesis process and the role of each chemical are as follows. Sucrose and PVA were used due to their relative ease for forming complexes. Sucrose was used as a fuel for the reaction, and PVA was used as a polymeric stabilizer, as portrayed in Fig. 5 [41,42]. PVA was used because of its biocompatibility and biodegradability [43]. Sucrose was decomposed into glucose and fructose (Fig. 5a); thereafter, oxidation occurred, yielding saccharic acid. Then, the saccharic acid reacted to form a metal complex as a precursor for the particles (Fig. 5b). Further reactions occurred, where the saccharic acid underwent polyesterification with PVA and a complexed saccharic acid, resulting in the formation of a polymeric resin with dispersed metal cations (Fig. 5c).

Table 2
Geometric parameters of pure and Yb^{3+}-doped ZnO nanoparticles.

Sample (at. %)	Bond length (Zn—O) Å	*R*	Volume (V) $(Å)^3$ ± 5%	Atomic packing factor (c/a)
ZnO	1.939	1.018	48.66	1.603
ZnO:Yb 1	1.930	1.020	47.90	1.600
ZnO:Yb 5	1.927	1.018	47.78	1.604
ZnO:Yb 10	1.924	1.021	47.48	1.600

The FTIR spectra from 4000 cm^{-1} to 650 cm^{-1} were measured to evaluate the composition of Zn1-xYbxO (0, 1, 5, 10 at.%) nanoparticles prepared using PVA/sucrose by the solution method and calcined at 450 °C. The comparison of the obtained spectra is shown in Fig. 6. All the samples exhibited absorption bands at 3404, 1715, 1639, 1514, 1398, 1219, 838 and 679 cm^{-1}. The bands at approximately 1639 cm^{-1} and 679 cm^{-1} were attributed to Zn—O stretching modes in the ZnO lattice [44]. The bands observed at approximately 3404 cm^{-1} and 1715 cm^{-1} were attributed to the stretching vibrations of -OH (hydroxyl groups) and C═O (carbonyl groups) [45]. For ZnO nanoparticles, the —OH bands exhibited lower intensity=, which is related to the degree of bonded bands. The absorption band located at approximately 1514 cm^{-1} corresponds to the stretching vibration of C═C. At approximately 1398 cm^{-1}, a band attributed to the bending vibration of C—O—H (from sucrose) is observed. The band associated with the C—O stretching vibration is observed at 1219 cm^{-1}, which can be attributed to secondary alcohol groups. The characteristic absorption band for the C—C stretching vibration is located at approximately 838 cm^{-1} [46].

3.3. FESEM and HRTEM analysis

To observe the effect of the synthesis route and ytterbium content (at. %) on the surface morphology of the $Zn_{1-x}Yb_xO$ (0, 1, 5, 10 at.%) nanoparticles, FESEM analyses were performed. The results are shown in Fig. 7. The resulting morphology of the ZnO and Yb-doped ZnO nanoparticles can be interpreted as follows: polyesterification occurred during the synthesis process when the precursor solution was heated, followed by combustion, where carbon dioxide and water were produced, as portrayed in Eq. (8). This led to the development of porosity in the nanoparticles.

$$C_{12}H_{22}O_{11} + 12O_2 \rightarrow 12CO_2 + 11H_2O \tag{8}$$

After 1 mol of sucrose was decomposed, 23 mol of gases were liberated. Consequently, the large volume of gases produced during the synthesis process generated the observed microstructure. No significant change in surface morphology was observed.

Complete analysis of the ZnO nanoparticles was performed using TEM/HRTEM/STEM. Fig. 8a shows a low-magnification image of ZnO nanoparticles, which was recorded to obtain a panoramic profile of the ZnO nanoparticles. The inset in this image shows a relative frequency histogram of the crystallite size distribution, where an average crystallite size of 25 nm was obtained. This value is close to that obtained by XRD analysis. Fig. 8b and c show high-resolution TEM images of ZnO nanoparticles. Fig. 8c shows the lattice fringes of ZnO with an interplanar spacing of $d = 0.26$ nm, which matches the interplanar distances between the (002) crystal planes of ZnO. Fig. 8d illustrates a similar distribution of Zn and O inside nanoparticles. Fig. 8(e–i) shows the STEM images of the ZnO nanoparticles. The differences in the contrast in the HAADF-STEM images are dominated by Rutherford scattering [47]. The scattering intensity is due to the atomic numbers of elements (Zn = 30 and O = 8) in the material. To acquire the mapping images, the k-line spectra of the elements were used. The elemental mapping images of the nanoparticles are presented in Fig. 8(g–i). The green and red color images correspond to O and Zn, respectively. The last image is an overlap of the O and Zn images.

3.4. BET surface measurements

To study the specific surface areas and pore volume of the $Zn_{1-x}Yb_xO$ (0, 1, 5, 10 at.%) nanoparticles, gas sorption was analyzed by the BET method. The nitrogen adsorption/desorption isotherms and pore size distribution plots of the ytterbium-doped and undoped ZnO nanoparticles are shown in Fig. 9. All the isotherms exhibit a type IV curve according to the IUPAC classification [48]. Additionally, a type H3

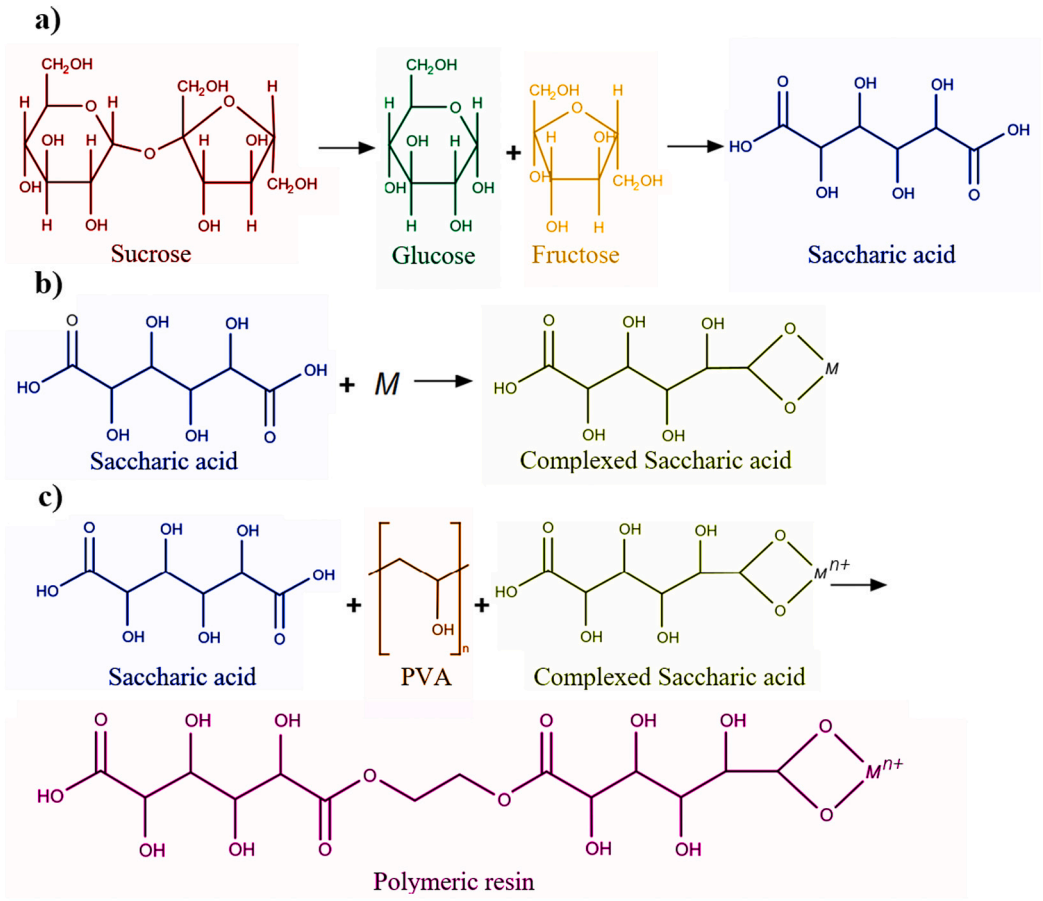

Fig. 5. Reactions involved in the formation of a polymeric resin from sucrose and PVA.

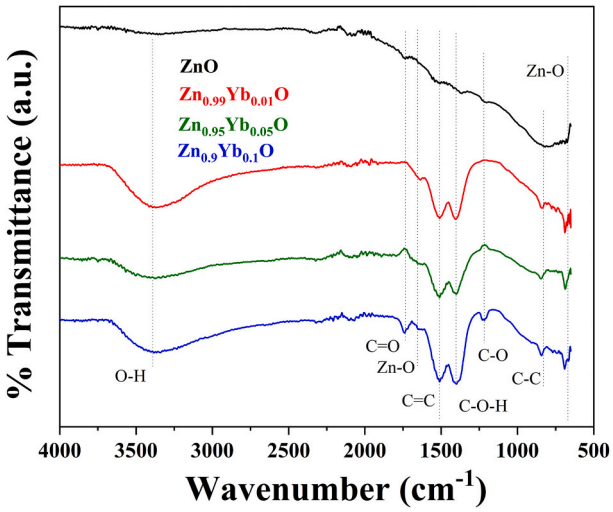

Fig. 6. FTIR spectra of $Zn_{1-x}Yb_xO$ (0, 1, 5, 10 at.%) nanoparticles.

hysteresis loop is observed for all the particles, and this behavior is related to mesoporous materials. The calculated surface areas are 24.91, 128.92, 56.53, and 94.31 $m^2\ g^{-1}$, and the relative pore volumes are 0.067, 0.207, 0.085, and 0.158 $cm^3\ g^{-1}$ for the $Zn_{1-x}Yb_xO$ (0, 1, 5, 10 at.%) nanoparticles, respectively. The results show that ytterbium-doped nanoparticles exhibited a higher surface owing to the smaller crystallite size of undoped ZnO nanoparticles, which agrees with the previous XRD and HTREM analysis results. Fig. 9b shows the Barret-Joyner-Halenda (BHJ) pore size distributions of the $Zn_{1-x}Yb_xO$ (0, 1, 5, 10 at.%) nanoparticles. The mean pore sizes are 10.80, 6.42, 6.02 and 6.45 nm for $Zn_{1-x}Yb_xO$ (0, 1, 5, 10 at.%) nanoparticles, respectively. The average pore diameters are all less than 50 nm, consistent with a mesoporous material. The ZnO particles exhibited a lower surface area and pore volume, which may be a consequence of nanoparticle agglomeration, as seen in the FESEM results.

3.5. UV–visible absorption spectroscopy

To investigate the optical properties of $Zn_{1-x}Yb_xO$ (0, 1, 5, 10 at.%) nanoparticles, UV–visible absorption spectroscopy analyses were carried out. The spectra were recorded in the wavelength range of 200–800 nm, and the results are shown in Fig. 10. The variations in the absorbance spectra were caused by defects in features such as the grain structure, crystallite size, and oxygen vacancies, among others. The samples exhibited an absorption edge at approximately 370–380 nm, which is related to the optical transition of electrons from the valence band (VB) to the conduction band (CB). The spectra of the doped ZnO nanoparticles exhibited a slight blueshift with respect to those of the undoped ZnO nanoparticles. The absorbance spectra were converted to the Kubelka-Munk function as follows [49]:

$$F(R_\infty) = \frac{(1 - R_\infty)^2}{2R_\infty} \tag{9}$$

where R is the absolute reflectance. Using Tauc's relation $(\alpha h\nu) = A(h\nu - E_g)^n$, the band gap energy was calculated, considering a direct transition (n = 1/2) and $\alpha \sim F(R)$. Fig. 10b shows a slight increase in the band gap with an increase in the Yb^{3+} doping content, which can be ascribed to the Moss-Burstein effect [50]. This effect is related to a change in the charge carrier density. A free charge carrier was released

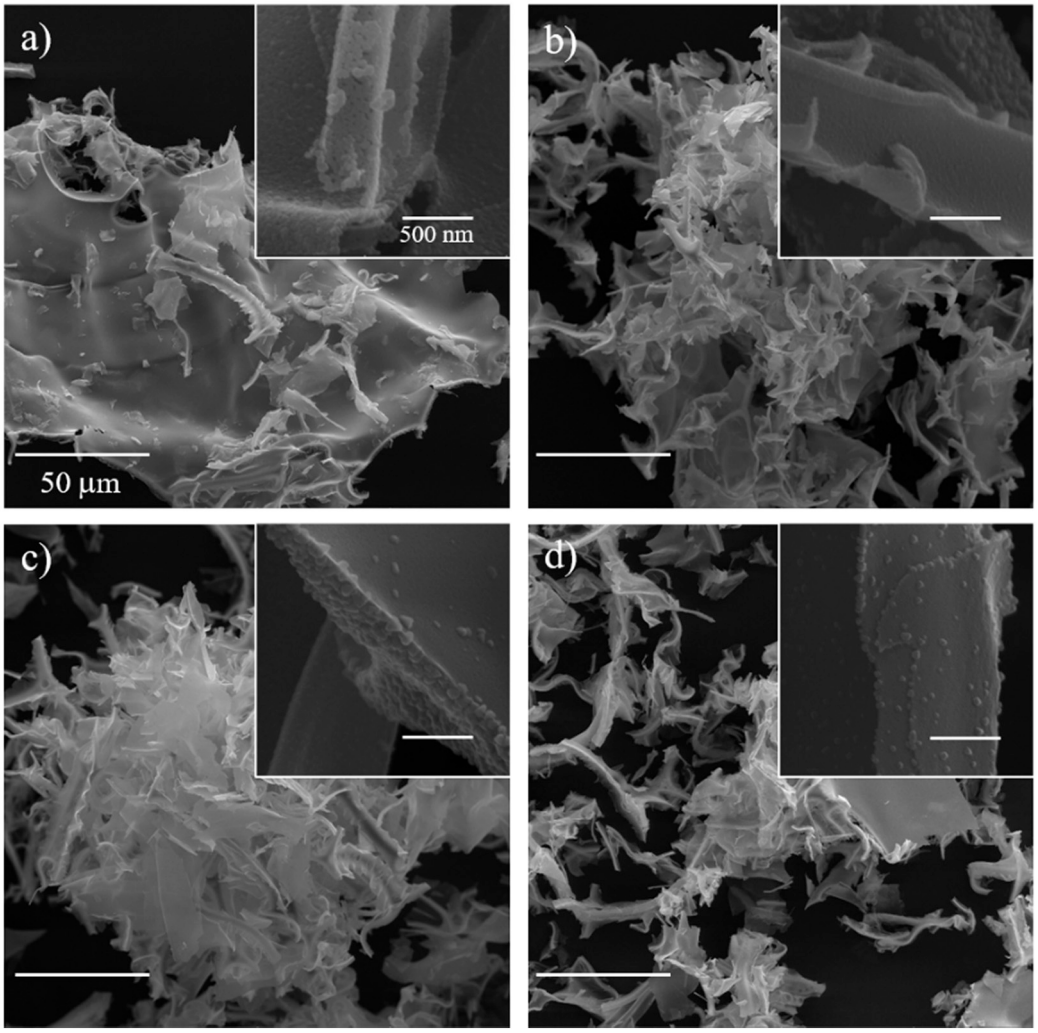

Fig. 7. FESEM images of a) ZnO, b) $Zn_{0.99}Yb_{0.01}O$, c) $Zn_{0.95}Yb_{0.05}O$ and d) $Zn_{0.9}Yb_{0.1}O$.

when Zn^{2+} ions were substituted by Yb^{3+} ions in the wurtzite structure. Some wide energy band gaps were reported when ZnO nanoparticles were doped with rare earth elements (REEs) [51,52]. According to the literature, the band gap of defect-free ZnO is 3.37 eV, and the value obtained in this work was lower than that of defect-free ZnO. This finding may be associated with an increase in cation or anion vacancies as a consequence of the synthesis method [52]. Some reports have proposed that an increase in the band gap is attributed to the quantum confinement effect due to crystallite size reduction as ytterbium is incorporated into ZnO nanoparticles. However, the exciton Bohr ratio of ZnO is 2.38 nm, and in this work, the smaller crystallite size was higher than this value, so the quantum effect in Yb-doped ZnO nanoparticles cannot explain the blueshift [53].

From the *Eg* values obtained above, the refractive index (*n*) was calculated using three different models, Ravindra et al. [54], Hervé and Vandamme [55] and Reddy and Anjayenulu [56], using the following equations:

$$n = 4.084 - 0.62E_g \tag{10}$$

$$n = \left(\frac{95}{E_g}\right)^{1/4} \tag{11}$$

$$n = \left(\frac{154}{E_g - 0.365}\right)^{1/4} \tag{12}$$

As shown in Fig. 11, the refractive index obtained is higher than 2 ($n > 2$), and the band bap values are higher than 3 ($E_g > 3$). According to Naccarato et al. [57] and the *n* and E_g values, the $Zn_{1-x}Yb_xO$ (0, 1, 5, 10 at.%) nanoparticles are classified as TMs (transition metals) with an empty *d* shell (V^{5+}). These results show the potential application of these nanoparticles as sensors and optoelectronic devices. The high refractive index corresponds to ZnO and $Zn_{0.99}Yb_{0.01}O$ nanoparticles, whereas the lower value corresponds to $Zn_{0.1}Yb_{0.1}O$ nanoparticles. The three different models exhibited a similar pattern.

3.6. XPS analysis

The surface chemistry of the $Zn_{1-x}Yb_xO$ (x = 0, 1, 5, 10) nanoparticles was evaluated by XPS. For this analysis, the photoemission intensity was analyzed by employing AAnalyzer® software [58]. Fig. 12 shows the O 1*s*, Zn 2*p*, Yb 4*d* and C 1*s* core levels for the $Zn_{1-x}Yb_xO$ powders according to the Yb concentration. To correct the charge effect, the high-resolution XPS spectra were aligned to the C 1*s* peak centered at 284.8 eV. The fitting process was carried out using Voigt-type profiles that are a convolution of a Lorentz-type profile and a Gaussian-type profile. The Zn 2*p* core level was fitted by employing a double Lorentzian-type profile for photoemission signals with intrinsic asymmetry. Fig. 12a shows the O 1*s* signals that were fitted with three singlet peaks related to O^{2-} ions coordinated with Zn^{2+} ions in the ZnO crystal lattice, hydroxyl groups (—OH) and near-surface oxygen (C═O bonds). The hydroxyl

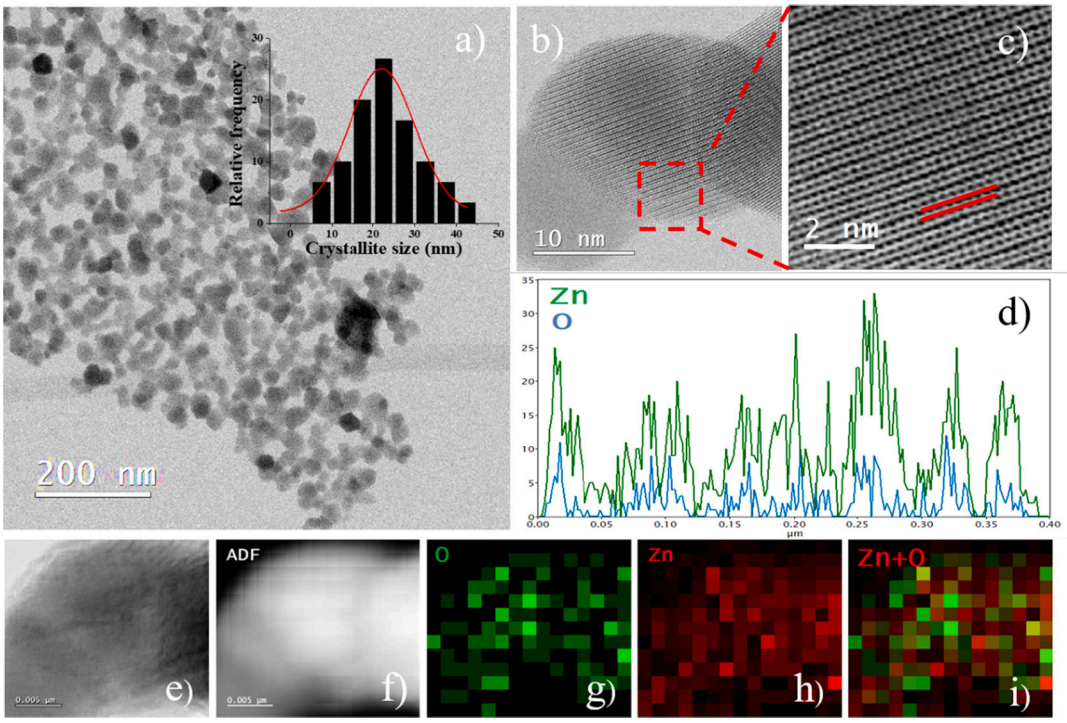

Fig. 8. ZnO nanoparticles. a) TEM image (inset: crystallite size distribution histogram), (b, c) HRTEM images, d) elemental profile in STEM mode, (e, f) HAADF image, energy-dispersive X-ray spectroscopy (EDS) element maps of *O* (g) and *Zn* (h), composite EDS map of *O* and *Zn* (i).

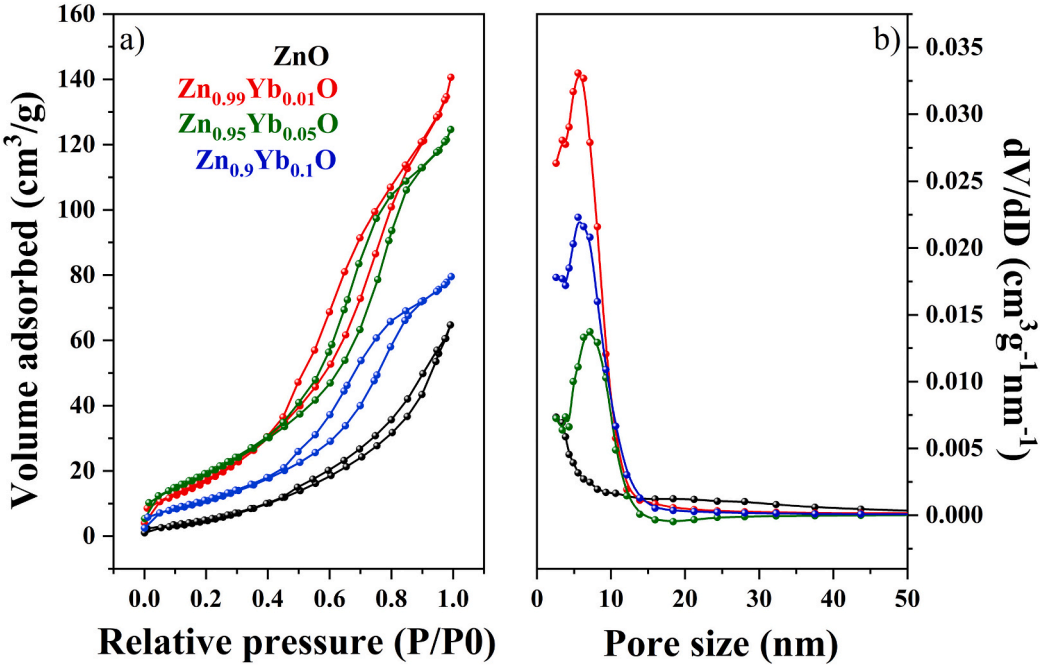

Fig. 9. a) N_2 adsorption/desorption isotherms and b) pore size distribution calculated from the adsorption branch by the BJH model of $Zn_{1-x}Yb_xO$ (0, 1, 5, 10 at.%) nanoparticles.

groups are associated with functional groups from sucrose, which was used as a fuel in the combustion reaction during synthesis. Fig. 12b illustrates the Zn 2*p* spectra, where it is possible to observe the $2p_{3/2}$ and $2p_{1/2}$ branches with a spin-orbit splitting of 23.1 eV. The spectra were fitted using one doublet centered at 1021.45 eV, which was associated with Zn^{2+} ions in the ZnO crystal lattice. Additionally, at high binding energies, two singlet peaks (Gaussian-type profile) associated with plasmon losses (1033.83 eV and 1040.0 eV) are observed, which are characteristics of the wurtzite-type crystal structure [59]. Fig. 12c shows the Yb 4*d* core level fitted with two doublet peaks with a spin-orbit splitting of approximately 13.44 eV. The former, associated with Yb^{3+} ions, includes a $4d_{5/2}$ branch and a $4d_{3/2}$ branch centered at 185.46 eV and 198.90 eV, respectively. The latter, with features centered at 192.13 eV ($4d_{5/2}$) and 205.56 eV ($4d_{3/2}$), was related to a satellite peak

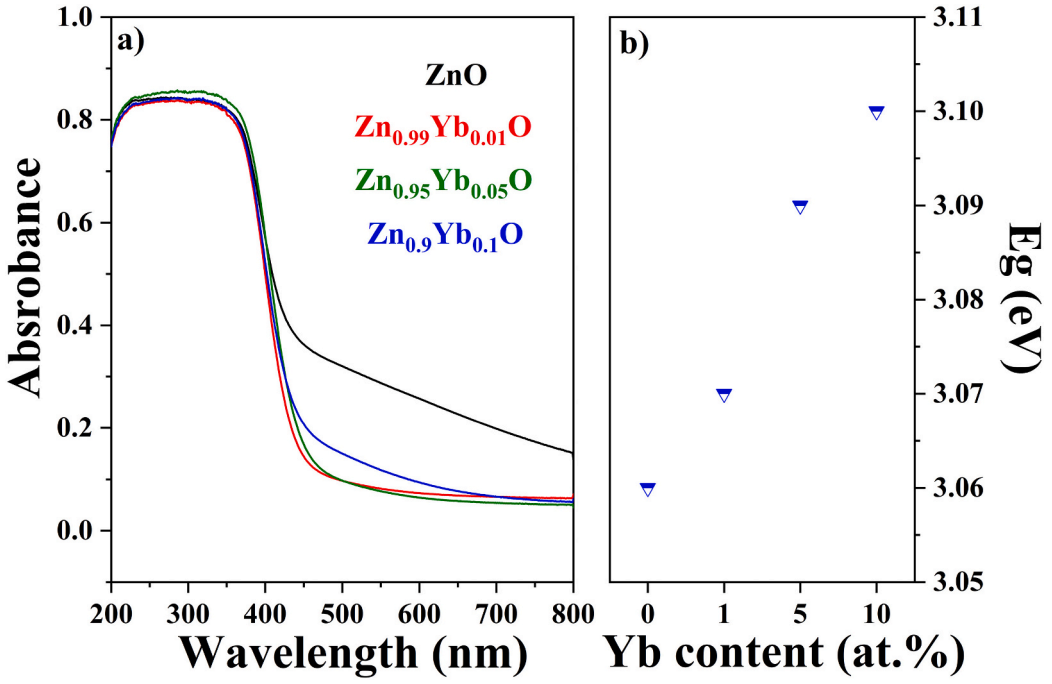

Fig. 10. UV–visible absorbance spectra of the $Zn_{1-x}Yb_xO$ (0, 1, 5, 10 at.%) nanoparticles. b) Effect of the ytterbium content (at.%) on the optical band gap of the ZnO nanoparticles.

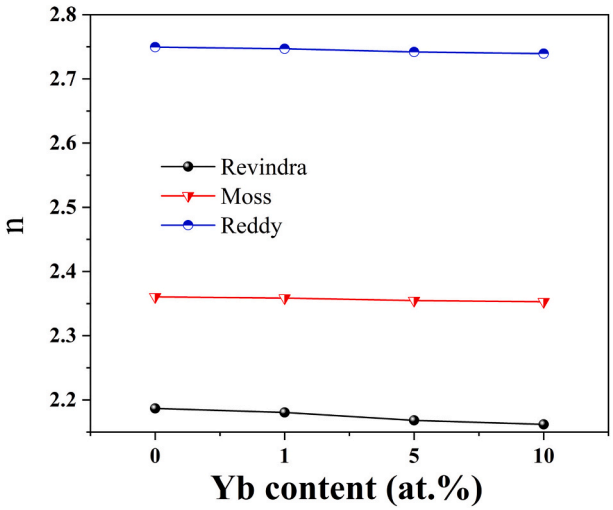

Fig. 11. Refractive index of $Zn_{1-x}Yb_xO$ (0, 1, 5, 10 at.%) nanoparticles calculated using different models. The plot shows the refractive index as a function of Yb content (at.%).

(Table 3) [60–62].

3.7. Antibacterial assays

Antibacterial activity assays of Zn1-xYbxO (0, 1, 5, 10 at.%) nanoparticles were performed against *S. aureus* (gram-positive) and *E. coli* (gram-negative). A difference in the antimicrobial effect was observed between the two bacterial strains, with a greater effect observed for *S. aureus*. Interestingly, the antimicrobial effect of the doped ZnO nanoparticles decreased when compared to that of ZnO nanoparticles. At a concentration of 1 mg/mL, all the treatments displayed the most significant effect on reducing the biomass density for both bacterial strains (Fig. 13). When the treatment was done with a dilution whose concentration was 1 mg/mL, the *S. aureus* was affected significantly, regardless of the type of nanoparticles. Differently, *E. coli* showed biomass development in all dilutions exposed to $Zn_{0.9}Yb_{0.1}O$ at the same concentration. Finally, although the *E. coli* development in the biomass was compromised by all the treatments when compared to the positive control, the development of *S. aureus* was affected more drastically.

The effect of the nanoparticles on the bacterial growth over time was also evaluated. Statistical analysis of the kinetics was carried out using an independent-samples *t*-test. All assays were performed in triplicate, and the significance level was set at $P < 0.05$. A statistical analysis demonstrated that the use of nanoparticles decreased the aerobic development and cell proliferation, resulting in a deficit in sigmoid growth in both bacterial strains. The cellular biomass phenotype was also quantified, and as the percentage of ytterbium content increased, a negative impact on the antimicrobial properties was observed (see Fig. 14).

To understand the antimicrobial effects of the $Zn_{1-x}Yb_xO$ (0, 1, 5, 10 at.%), nanoparticles, different mechanisms, such as photocatalyst activity, electrostatic interactions, metal ion release, membrane damage and reactive oxygen species (ROS), have been proposed [63]. It has been determined that the antimicrobial activity of ZnO nanoparticles principally follows the ROS mechanism described in the following reactions:

$$Zn - Yb - O + hv \rightarrow e^- + h^+$$

$$h^+ + H_2O \rightarrow {}^{\circ}OH + H^+$$

$$e^- + O_2 \rightarrow {}^{\circ}O_2^-$$

$${}^{\circ}O_2^- + H^+ \rightarrow HO_2^{\circ}$$

$$HO_2^{\circ} + H^+ + e^- \rightarrow H_2O_2$$

When nanoparticles are exposed to UV excitation, superoxide anion radicals ($^{\circ}O_2$) are produced by the reaction of electrons with oxygen. Afterwards, hydroxyl radicals ($^{\circ}OH$) are formed by the attraction of electrons from water due to a hole in the VB. Finally, hydrogen peroxide (H_2O_2) is formed in the reaction between superoxide anions and

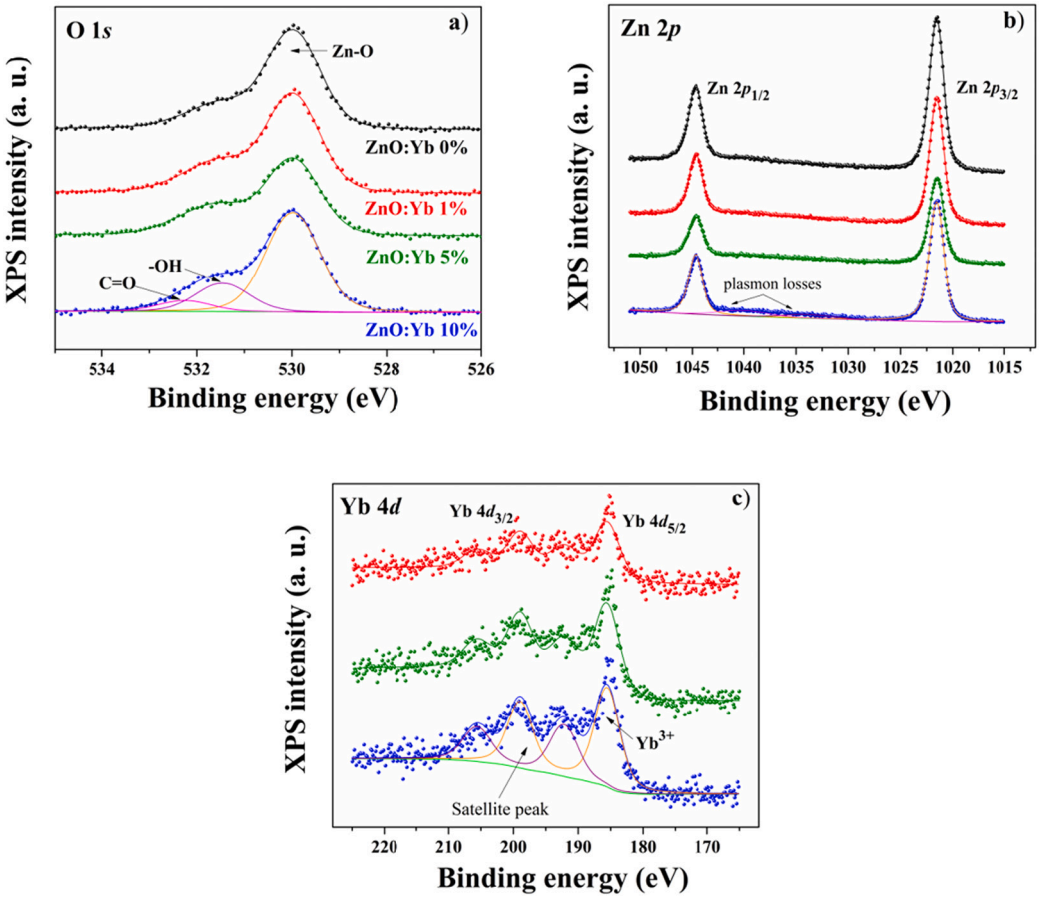

Fig. 12. High-resolution spectra of a) O 1*s*, b) Zn 1*p*, and c) Yb 4*d* core levels for the Yb-doped ZnO powders.

Table 3
Atomic concentrations of Zn, O, and Yb present in the samples.

Sample	Zn (at.%)	O (at.%)	Zn/O	Yb (at.%)
0	35.14	34.42	1.02	0
1	24.78	28.79	0.86	4.32
5	17.72	23.97	0.76	6.87
10	24.45	30.01	0.81	7.93

electron–hole pairs. This antimicrobial mechanism is shown in Fig. 15. Additionally, superoxide anions and hydroxyl radicals cannot penetrate the cell membrane, but they cause lipid, nucleic acid and carbohydrate damage. Additionally, H_2O_2 is capable of penetrating the bacterial cell membrane, causing damage, preventing bacterial growth and eventually eliminating the bacterial population. A decrease in the bacterial growth due to the liberation of heavy metal ions such as Zn^{2+} and Yb^{3+} used in this research has been reported [64]. The $Zn_{1-x}Yb_xO$ (0, 1, 5, 10 at.%) nanoparticles are positively charged, whereas the bacterial cells are negatively charged; under these conditions, an electrostatic force occurs, and metal ions enter the cells and interact with the -SH groups of the surface proteins of bacterial cells [65]. Subsequently, most of the proteins involved in biological processes are inactivated, resulting in bacterial death.

Different rare-earth-doped ZnO nanoparticles have been reported to have a better antimicrobial activity when compared to undoped nanoparticles [11,12,35]. Previous research has determined that rare earth incorporation onto ZnO nanoparticles reduces the crystallite size and consequently results in a larger amount of ROS production, thus increasing the antimicrobial activity. Additionally, it has been reported that, although unrelated to biocidal activity, ZnO nanoparticles doped with Nd^{3+} have an enhanced antimicrobial activity, related to the crystallite size [66]. This is a key factor; a small particle exhibits a higher specific surface area, and more ROS are present. In this work, ytterbium-doped ZnO nanoparticles exhibited smaller particle sizes than ZnO nanoparticles.

To counteract the effect of the stress induced by ROS, bacteria have tightly regulated genetic mechanisms, which correspond to the extensively studied biogenesis systems of the Fe—S cluster located in different operons. In bacteria, there are three Fe—S cluster synthesis machineries that have been extensively described: SUF (sulfur mobilization), Isc, and Nif; in terms of functionality, these systems may be redundant, but they are biochemically distinct [67–69]. *S. aureus* relies on the SufCDSUB machinery for the synthesis of Fe—S clusters from monoatomic Fe^{2+}, S0, and electrons [70]. Since *S. aureus* has a genetic system for protection purposes only, this could be the reason for its susceptibility to adapt to oxidizing conditions in the environment when compared to *E. coli*; however, this hypothesis must be validated experimentally. In *E. coli,* the participation of the ISC and SUF operons has been demonstrated by means of a transcriptomic analysis in which the bacteria were exposed to silver nanoparticles that induced a significant increase in the expression of both systems [71]; this could result in an increase in tolerance to the presence of ROS, as observed in the phenotypes obtained under the evaluated treatments.

In the case of *S. aureus*, performed essays determined that the antimicrobial activity depends more on the particle size, making it more susceptible to the production of ROS (Fig. 14a) [72]. By analyzing XRD results, it was inferred that the crystallite size of ZnO is twice the size of ytterbium-doped ZnO nanoparticles, suggesting that the difference observed in the antimicrobial effect can be caused by this variation. The formulated nanoparticles attach to the cell membrane; therefore, small

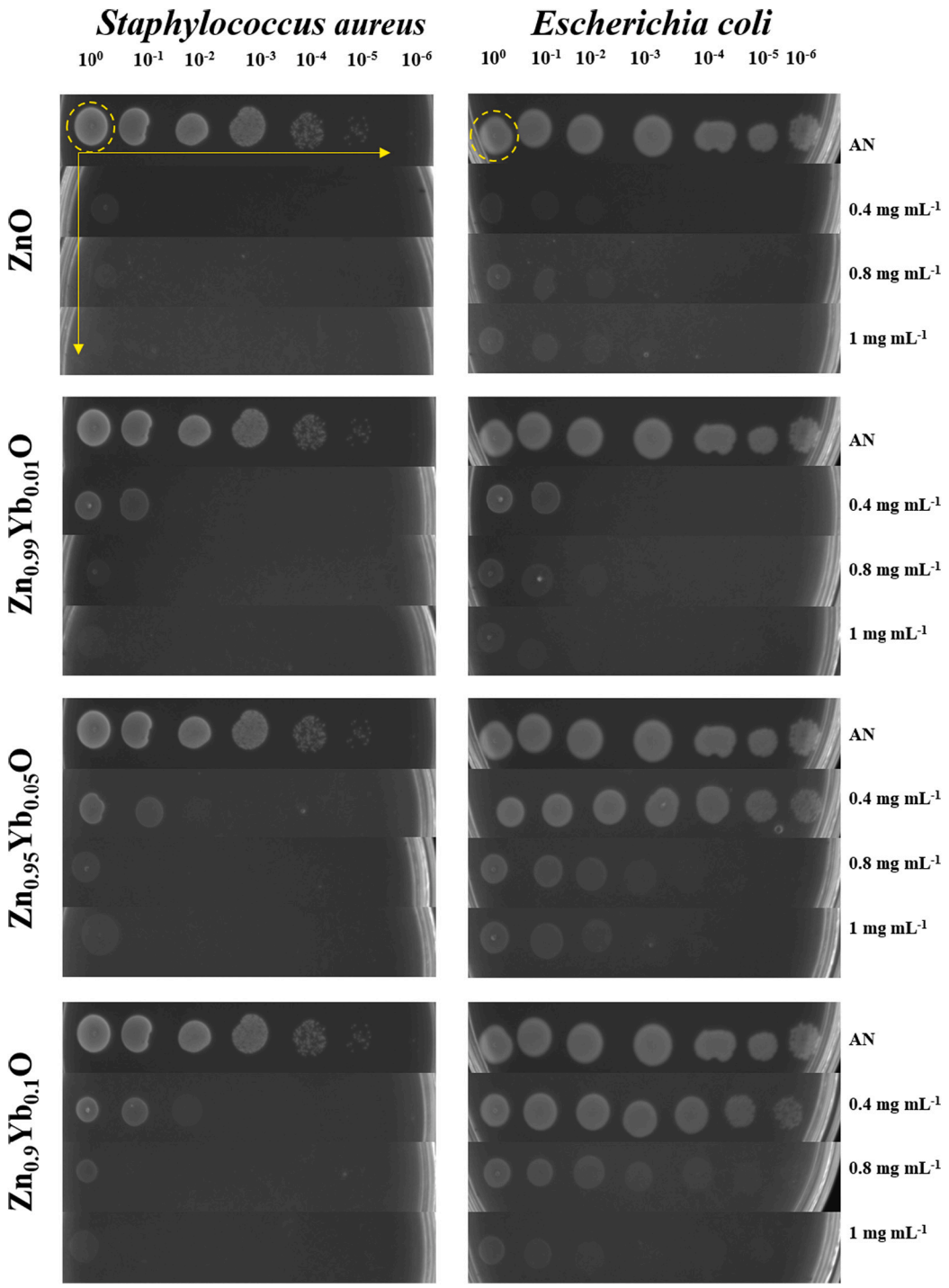

Fig. 13. Antimicrobial activity effect of nanoparticles on the bacterial growth phenotype.

nanoparticles cover a larger surface of the cell membrane increasing ROS levels; consequently, antimicrobial activity is increased. In this work, the Yb-doped ZnO nanoparticles exhibited a slightly improved bioactivity (for *S. aureus*) when compared with ZnO nanoparticles. In contrast, antimicrobial effects on *E. coli* are dose-dependent; this is due to electrostatic interaction between bacteria-nanoparticles. It has been widely reported that nanoparticles produce cell membrane damage and eventual bacterial death [73]. XPS results show that the Zn/O ratio decreases as ytterbium content increases, producing a larger amount of Zn^{2+} vacancies and consequently, a decreasing antimicrobial activity in this strain. Additionally, it has been reported that a decrease in the metal-doped ZnO bandgap is capable of improving antimicrobial activity [74]. UV–vis results depict the increase of $Zn_{1-x}Yb_xO$ (0, 1, 5, 10 at.%) nanoparticles bandgap in parallel to ytterbium increase, producing an observable decrease in antimicrobial activity.

3.8. ANNs and absorbance estimation

Machine learning (ML) is an area of artificial intelligence that has been applied recently to areas such as biotechnology and material science to discover patterns that are otherwise difficult to find and translate into computer programs [75–77]. In this work, we used the supervised learning approach. Supervised learning tries to discover the relationship between input attributes and a target or dependent variable. This

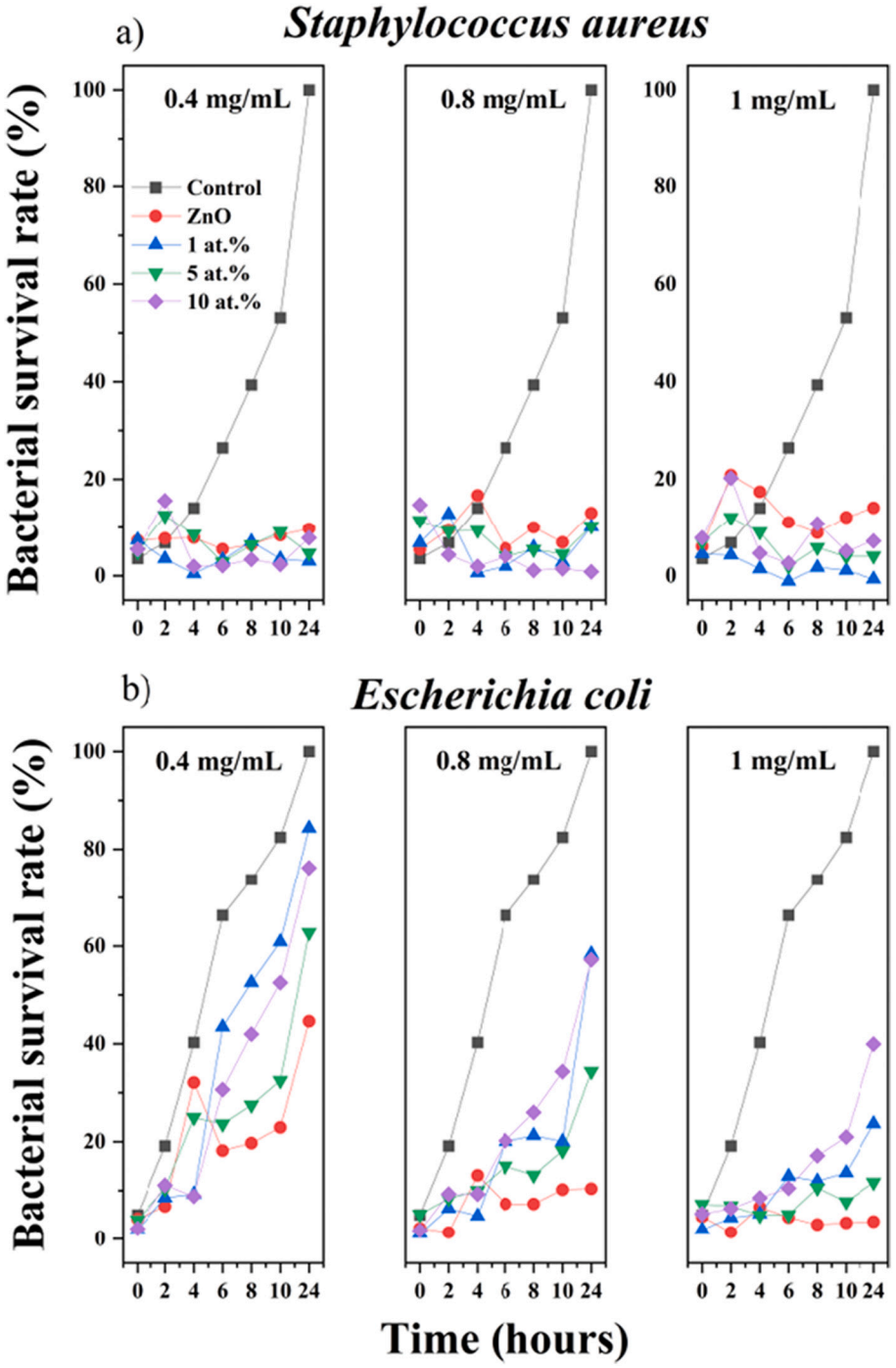

Fig. 14. Antibacterial rate of a) *S. aureus* and b) *E. coli* when are exposed to $Zn_{1-x}Yb_xO$ (0, 1, 5, 10 at.%) nanoparticles.

approach requires instances in which the value of the target is known for a given combination of values of the attributes. These cases are used to train a model. The model represents a phenomenon that was embedded in the dataset. Such a model can be used to predict the value of the output attribute when the values of the features are known. There are several types of supervised learning algorithms. To test the applicability of such an approach in this problem, we used an ANN. ANNs are inspired by the functioning of the human brain [78]. Fig. 16a shows the basic structure of an artificial neuron. Vector xi denotes the attributes, and the weights of the connections are given by wi, where the special case w_0 is called bias. The function f(…) is called the activation function and can take several forms. The value y is the output. Finally, an ANN is a group of neurons organized in levels, as illustrated in Fig. 16b. The training process involves adjusting the set of weights using an optimization algorithm, also called the solver.

The problem we are interested in solving here is as follows. Given four attributes, is it possible to predict the inhibition of the growth of certain bacteria? The attributes considered are treatment time, atomic concentration, concentration of the nanoparticle and type of bacteria. The response or target is the absorbance of the sample, which indirectly indicates whether or not the nanoparticle under such conditions was able to inhibit the growth of the bacteria. The dataset was composed of 630 samples in total. Table 4 shows the structure of the dataset.

The computational experiments were performed using Orange Toolbox [79], which provides a graphical interface to define the workflow. Fig. 17 presents the setup used to gather the results. Regarding the

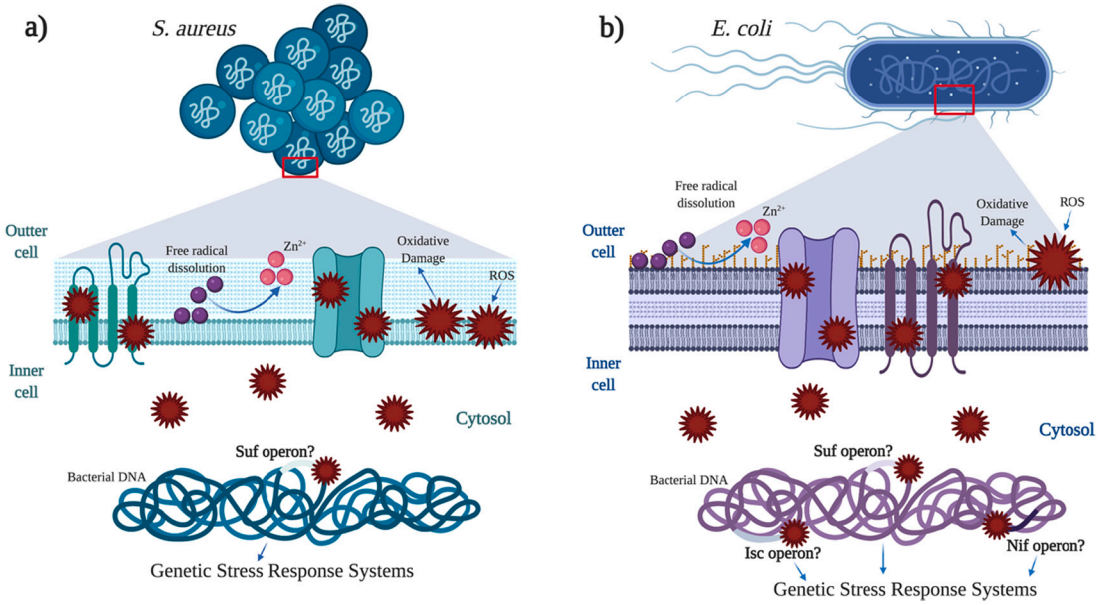

Fig. 15. Schematic representation of a possible antibacterial mechanism of $Zn_{1-x}Yb_xO$ (0, 1, 5, 10 at.%) nanoparticles.

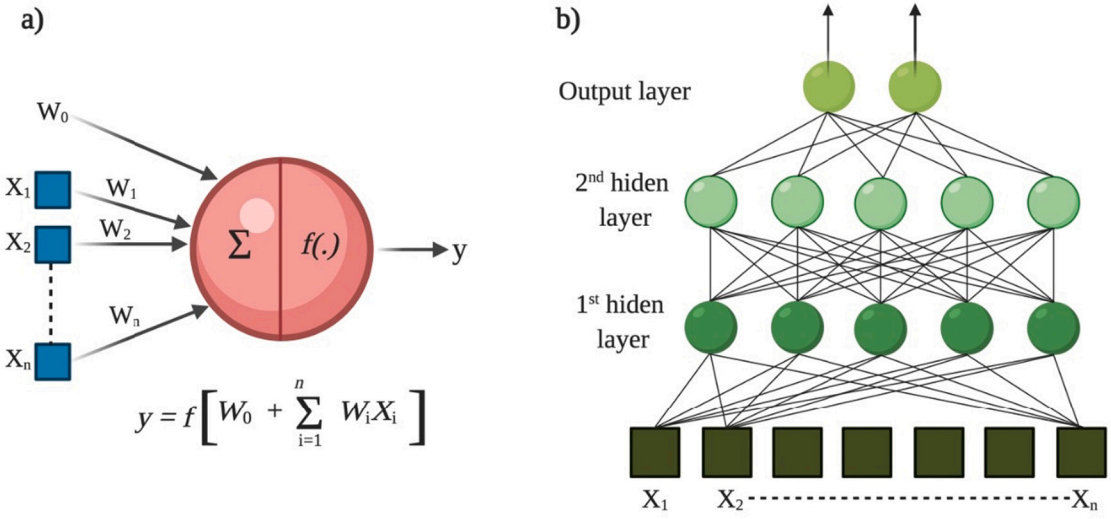

Fig. 16. ANN architecture.

Table 4
Attributes of the records gathered in the dataset.

Attribute	Type	Values
Time	Real	{0,2,4,6,8,10,24}
Type	Categorical	{1,2,3,4,5}
Concentration	Real	{400, 800, 1000}
Bacteria	Categorical	{1,2}

parameters for the ANN, four activation functions were used: ReLu, Identity, Logistic and Tanh and the solver L-BFGS-B.

The performance of the method was evaluated by computing the following metrics: root mean square error (RMSE), mean absolute error (MAE) and coefficient of determination (R^2). Table 5 presents the results of the neural network for *S. aureus,* and Table 6 shows the results for *E. coli*. The best result is marked in bold. In the case of *S. aureus,* it was possible to obtain a good representation of the data (as indicated by R^2 = 0.929) with 5 neurons and an error of approximately 1%. For *E. coli,* the best result required 40 neurons, R^2 = 0.97, and the error was approximately 2%. The error in both cases is acceptable.

4. Conclusions

In this work, pure and ytterbium-doped ZnO nanoparticles, $Zn_{1-x}Yb_xO$ ($0.0 \leq x \leq 0.1$) were successfully synthesized by a solution-polymerization method. The average crystallite size remained under 20 nm for all the samples. Results indicated that as ytterbium ions increased, a slight decrease in structural parameters was observed and compressive stress was developed. The optical band gap values blue-shifted after ytterbium incorporation onto ZnO, which was explained by the Moss-Burstein effect. Also, a variation in the Zn/O ratio, which is related to vacancy formation with ytterbium incorporation onto ZnO, was observed. The antimicrobial effect of $Zn_{1-x}Yb_xO$ nanoparticles was supported by statistical data analysis. According with antimicrobial essays, two behaviors were observed: *S. aureus* is more susceptible to particle size while *E. coli* bioactivity was improved by increasing nanoparticles concentration. These results suggest that the antimicrobial activity of the nanoparticles reported in this work mainly follows the

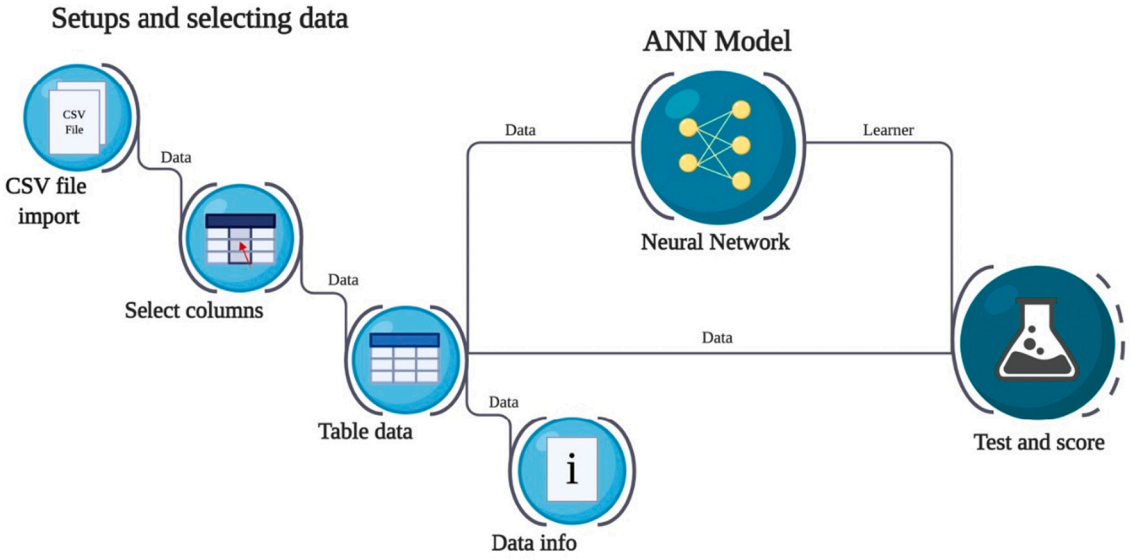

Fig. 17. Experimental setup in Orange indicating that the model could be used to forecast new values of absorbance with good precision.

Table 5
Neural network results for *S. aureus*. In all cases, $\alpha = 0.0001$, the solver used is L-BFGS-B, and the maximum number of iterations was set to 200, except in the last row, where it was 40.

Hidden neurons	Activation	RMSE	MAE	R^2
100	ReLu	0.012	0.009	0.945
50	ReLu	0.013	0.010	0.934
150	ReLu	0.012	0.009	0.940
25	ReLu	0.013	0.010	0.929
15	ReLu	0.013	0.010	0.928
5	ReLu	0.013	0.010	0.929
5	Identity	0.042	0.030	0.288
5	Logistic	0.042	0.030	0.302
5	Tanh	0.017	0.013	0.884
5	ReLu	0.013	0.010	0.929
5	**ReLu**	**0.013**	**0.010**	**0.929**

Table 6
Neural network results for *E. coli*. In all cases, $\alpha = 0.0001$, and the solver used is L-BFGS-B.

Hidden neurons	Activation	Max iter	RMSE	MAE	R^2
150	ReLu	100	0.015	0.011	0.983
100	ReLu	100	0.018	0.013	0.976
75	ReLu	100	0.019	0.014	0.973
50	ReLu	100	0.020	0.015	0.969
25	ReLu	100	0.031	0.024	0.927
40	**ReLu**	**100**	**0.020**	**0.015**	**0.97**
40	Identity	100	0.084	0.064	0.47
40	Logistic	100	0.084	0.064	0.468
40	tanh	100	0.045	0.035	0.847
40	ReLu	90	0.022	0.017	0.965
40	ReLu	100	0.021	0.016	0.967

reactive oxygen species mechanism. The obtained results suggest that the synthesized nanoparticles may offer a new approach for the treatment of bacterial infection that may reduce some common side effects. With the experimental results obtained in the laboratory, an ML model was trained and evaluated. The model was built using an ANN and had an acceptable performance (1–2% error). The resulting mathematical structure can be used to better plan future experiments, saving time and resources.

CRediT authorship contribution statement

Diego Eloyr Navarro-López: Conceptualization, Investigation, Formal analysis. **Rebeca Garcia-Varela:** Investigation, Writing – original draft. **O. Ceballos-Sanchez:** Investigation, Writing – review & editing. **A. Sanchez-Martinez:** Investigation, Visualization. **Gildardo Sanchez-Ante:** Software, Validation, Writing – review & editing. **Kaled Corona-Romero:** Software, Validation. **D.A. Buentello-Montoya:** Software, Visualization, Writing – review & editing. **Alex Elías-Zuñiga:** Investigation, Formal analysis. **Edgar R. López-Mena:** Conceptualization, Investigation, Writing – review & editing.

Declaration of competing interest

The authors declare that they have no known competing financial interests or personal relationships that could have appeared to influence the work reported in this paper.

Acknowledgments

This work was partially funded by COECYTJAL through FODECYJAL Program and Tecnologico de Monterrey, Campus Monterrey, through the Research Chair in Nanotechnology and Devices Design. O. Ceballos-Sanchez acknowledges to Universidad de Guadalajara for the valuable financial support through the PRO-SNI 2020 and 511-6/2020-7045 PRODEP projects.

References

[1] K. Kairyte, A. Kadys, Z. Luksiene, Antibacterial and antifungal activity of photoactivated ZnO nanoparticles in suspension, J. Photochem. Photobiol. B Biol. 128 (2013) 78–84, https://doi.org/10.1016/j.jphotobiol.2013.07.017.
[2] J. Pasquet, Y. Chevalier, E. Couval, D. Bouvier, G. Noizet, C. Morlière, M. A. Bolzinger, Antimicrobial activity of zinc oxide particles on five micro-organisms of the challenge tests related to their physicochemical properties, Int. J. Pharm. 460 (2014) 92–100, https://doi.org/10.1016/j.ijpharm.2013.10.031.
[3] J. Sawai, Quantitative evaluation of antibacterial activities of metallic oxide powders (ZnO, MgO and CaO) by conductimetric assay, J. Microbiol. Methods 54 (2003) 177–182, https://doi.org/10.1016/S0167-7012(03)00037-X.
[4] L. Armelao, D. Barreca, G. Bottaro, A. Gasparotto, C. Maccato, C. Maragno, E. Tondello, U.L. Štangar, M. Bergant, D. Mahne, Photocatalytic and antibacterial activity of TiO2 and Au/TiO2 nanosystems, Nanotechnology. 18 (2007), https://doi.org/10.1088/0957-4484/18/37/375709.
[5] H. Hu, W. Zhang, Y. Qiao, X. Jiang, X. Liu, C. Ding, Antibacterial activity and increased bone marrow stem cell functions of Zn-incorporated TiO2 coatings on titanium, Acta Biomater. 8 (2012) 904–915, https://doi.org/10.1016/j.actbio.2011.09.031.

[6] U. Kadiyala, E.S. Turali-Emre, J.H. Bahng, N.A. Kotov, J. Scott Vanepps, Unexpected insights into antibacterial activity of zinc oxide nanoparticles against methicillin resistant: Staphylococcus aureus (MRSA), Nanoscale. 10 (2018) 4927–4939, https://doi.org/10.1039/c7nr08499d.
[7] R. García-Varela, R.M. García-García, B.A. Barba-Dávila, O.R. Fajardo-Ramírez, S. O. Serna-Saldívar, G.A. Cardineau, Antimicrobial activity of rhoeo discolor phenolic rich extracts determined by flow cytometry, Molecules. 20 (2015) 18685–18703, https://doi.org/10.3390/molecules201018685.
[8] K.E. Heiman, R.K. Mody, S.D. Johnson, P.M. Griffin, L. Hannah Gould, Escherichia coli O157 outbreaks in the United States, 2003–2012, Emerg. Infect. Dis. 21 (2015) 1293–1301, https://doi.org/10.3201/eid2108.141364.
[9] H.F.L. Wertheim, D.C. Melles, M.C. Vos, W. van Leeuwen, A. van Belkum, H. A. Verbrugh, J.L. Nouwen, The role of nasal carriage in Staphylococcus aureus infections, Lancet Infect. Dis. 5 (2005) 751–762, https://doi.org/10.1016/S1473-3099(05)70295-4.
[10] S.Y.C. Tong, J.S. Davis, E. Eichenberger, T.L. Holland, V.G. Fowler, Staphylococcus aureus infections: epidemiology, pathophysiology, clinical manifestations, and management, Clin. Microbiol. Rev. 28 (2015) 603–661, https://doi.org/10.1128/CMR.00134-14.
[11] M. Prathap Kumar, G.A. Suganya Josephine, G. Tamilarasan, A. Sivasamy, J. Sridevi, Rare earth doped semiconductor nanomaterials and its photocatalytic and antimicrobial activities, J. Environ. Chem. Eng. 6 (2018) 3907–3917, https://doi.org/10.1016/j.jece.2018.05.046.
[12] Z.N. Kayani, S. Sahar, S. Riaz, S. Naseem, Tuning of optical and antibacterial characteristics of ZnO thin films: role of Ce content, Ceram. Int. 45 (2019) 3930–3939, https://doi.org/10.1016/j.ceramint.2018.11.066.
[13] S. Anitha, S. Muthukumaran, Structural, optical and antibacterial investigation of La, Cu dual doped ZnO nanoparticles prepared by co-precipitation method, Mater. Sci. Eng. C. 108 (2020), 110387, https://doi.org/10.1016/j.msec.2019.110387.
[14] R. Perveen, S. Shujaat, Z. Qureshi, S. Nawaz, M.I. Khan, M. Iqbal, Green versus sol-gel synthesis of ZnO nanoparticles and antimicrobial activity evaluation against panel of pathogens, J. Mater. Res. Technol. 9 (2020) 7817–7827, https://doi.org/10.1016/j.jmrt.2020.05.004.
[15] A. Jain, R. Bhargava, P. Poddar, Probing interaction of Gram-positive and Gram-negative bacterial cells with ZnO nanorods, Mater. Sci. Eng. C. 33 (2013) 1247–1253, https://doi.org/10.1016/j.msec.2012.12.019.
[16] K. Velsankar, S. Sudhahar, G. Parvathy, R. Kaliammal, Effect of cytotoxicity and aAntibacterial activity of biosynthesis of ZnO hexagonal shaped nanoparticles by Echinochloa frumentacea grains extract as a reducing agent, Mater. Chem. Phys. 239 (2020), 121976, https://doi.org/10.1016/j.matchemphys.2019.121976.
[17] R.O. Yathisha, Y.A. Nayaka, Effect of solvents on structural, optical and electrical properties of ZnO nanoparticles synthesized by microwave heating route, Inorg. Chem. Commun. 115 (2020), 107877, https://doi.org/10.1016/j.inoche.2020.107877.
[18] R. Hong, T. Pan, J. Qian, H. Li, Synthesis and surface modification of ZnO nanoparticles, Chem. Eng. J. 119 (2006) 71–81, https://doi.org/10.1016/j.cej.2006.03.003.
[19] R.Y. Hong, J.H. Li, L.L. Chen, D.Q. Liu, H.Z. Li, Y. Zheng, J. Ding, Synthesis, surface modification and photocatalytic property of ZnO nanoparticles, Powder Technol. 189 (2009) 426–432, https://doi.org/10.1016/j.powtec.2008.07.004.
[20] S. Pokhriyal, S. Biswas, Effects of structural parameters on the optical and magnetic properties of surface stabilized intrinsic CdSe nanoparticles, Appl. Surf. Sci. 501 (2020), 144040, https://doi.org/10.1016/j.apsusc.2019.144040.
[21] H. Chen, J. Wang, X. Yin, C. Xing, J. Li, H. Qiao, F. Shi, Hydrothermal synthesis of BaTiO3 nanoparticles and role of PVA concentration in preparation, Mater. Res. Express 6 (2019), 55028, https://doi.org/10.1088/2053-1591/ab0520.
[22] T.K. Mandal, S. Ram, Synthesis of PbZr0.7Ti0.3O3 nanoparticles in a new tetragonal crystal structure with a polymer precursor, Mater. Lett. 57 (2003) 2432–2442, https://doi.org/10.1016/S0167-577X(02)01249-1.
[23] E.A. Cochran, D.-H. Park, M.G. Kast, L.J. Enman, C.K. Perkins, R.H. Mansergh, D. A. Keszler, D.W. Johnson, S.W. Boettcher, Role of combustion chemistry in low-temperature deposition of metal oxide thin films from solution, Chem. Mater. 29 (2017) 9480–9488, https://doi.org/10.1021/acs.chemmater.7b03618.
[24] M.M. Mallapur, B.K. Chougule, Synthesis, characterization and magnetic properties of nanocrystalline Ni-Zn-Co ferrites, Mater. Lett. 64 (2010) 231–234, https://doi.org/10.1016/j.matlet.2009.10.014.
[25] R. Al-Gaashani, S. Radiman, A.R. Daud, N. Tabet, Y. Al-Douri, XPS and optical studies of different morphologies of ZnO nanostructures prepared by microwave methods, Ceram. Int. 39 (2013) 2283–2292, https://doi.org/10.1016/j.ceramint.2012.08.075.
[26] A. Paul, H.N. Acharya, Equilibrium thermodynamics of nonstoichiometry in ZnO and aluminium doping of ZnO using aluminium chloride, J. Mater. Sci. 27 (1992) 1716–1722, https://doi.org/10.1007/BF01107195.
[27] F. Paraguay D., J. Morales, W. Estrada L., E. Andrade, M. Miki-Yoshida, Influence of Al, In, Cu, Fe and Sn dopants in the microstructure of zinc oxide thin films obtained by spray pyrolysis, Thin Solid Films 366 (2000) 16–27, https://doi.org/10.1016/S0040-6090(00)00752-5.
[28] K. Krunks, O. Bijakina, V. Mikli, T. Varema, E. Mellikov, Zinc oxide thin films by spray pyrolysis method, Phys. Scr. T. 79 (1999) 209–212, https://doi.org/10.1238/physica.topical.079a00209.
[29] D.J. Goyal, C. Agashe, M.G. Takwale, V.G. Bhide, S.K. Kulkarni, S. Mahamuni, Dopant induced modifications in the physical properties of sprayed ZnO: In films, J. Mater. Res. 8 (1993) 1052–1056, https://doi.org/10.1557/JMR.1993.1052.
[30] C. Mrabet, A. Boukhachem, M. Amlouk, T. Manoubi, Improvement of the optoelectronic properties of tin oxide transparent conductive thin films through lanthanum doping, J. Alloys Compd. 666 (2016) 392–405, https://doi.org/10.1016/j.jallcom.2016.01.104.
[31] S. Shanthi, N. Muthukumarasamy, S. Agilan, R. Balasundaraprabhu, Studies on Gd doped ZnO nanocrystalline thin films, Mater. Res. Innov. 19 (2015) 40–43, https://doi.org/10.1179/1433075X14Y.0000000199.
[32] T. Deepa Rani, K. Tamilarasan, E. Elangovan, S. Leela, K. Ramamurthi, K. Thangaraj, C. Himcinschi, I. Trenkmann, S. Schulze, M. Hietschold, A. Liebig, G. Salvan, D.R.T. Zahn, Structural and optical studies on Nd doped ZnO thin films, Superlattice. Microst. 77 (2015) 325–332, https://doi.org/10.1016/j.spmi.2014.10.001.
[33] M.M. Obeid, H.R. Jappor, K. Al-Marzoki, I.A. Al-Hydary, S.J. Edrees, M.M. Shukur, Unraveling the effect of Gd doping on the structural, optical, and magnetic properties of ZnO based diluted magnetic semiconductor nanorods, RSC Adv. 9 (2019) 33207–33221, https://doi.org/10.1039/c9ra04750f.
[34] A. Manikandan, E. Manikandan, B. Meenatchi, S. Vadivel, S.K. Jaganathan, R. Ladchumananandasivam, M. Henini, M. Maaza, J.S. Aanand, A.A. Othman, M. A. Ali, E.M.M. Ibrahim, M.A. Osman, Influence of Cu doping on structural, morphological, photoluminescence, and electrical properties of ZnO nanostructures synthesized by ice-bath assisted sonochemical method, J. Alloys Compd. 723 (2016) 399–411, https://doi.org/10.1016/j.jallcom.2016.05.131.
[35] A. Manikandan, E. Manikandan, B. Meenatchi, S. Vadivel, S.K. Jaganathan, R. Ladchumananandasivam, M. Henini, M. Maaza, J.S. Aanand, Rare earth element (REE) lanthanum doped zinc oxide (La: ZnO) nanomaterials: synthesis structural optical and antibacterial studies, J. Alloys Compd. 723 (2017) 1155–1161, https://doi.org/10.1016/j.jallcom.2017.06.336.
[36] A. Khorsand Zak, W.H. Abd Majid, M.E. Abrishami, R. Yousefi, X-ray analysis of ZnO nanoparticles by Williamson-Hall and size-strain plot methods, Solid State Sci. 13 (2011) 251–256, https://doi.org/10.1016/j.solidstatesciences.2010.11.024.
[37] F.I.H. Rhouma, F. Belkhiria, E. Bouzaiene, M. Daoudi, K. Taibi, J. Dhahri, R. Chtourou, The structure and photoluminescence of a ZnO phosphor synthesized by the sol gel method under praseodymium doping, RSC Adv. 9 (2019) 5205–5217, https://doi.org/10.1039/c8ra09939a.
[38] S. Sendhilnathan Hirthna, Enhancement in dielectric and magnetic properties of Mg2+ substituted highly porous super paramagnetic nickel ferrite nanoparticles with Williamson-Hall plots mechanistic view, Ceram. Int. 43 (2017) 15447–15453, https://doi.org/10.1016/j.ceramint.2017.08.090.
[39] M. Gaudon, O. Toulemonde, A. Demourgues, Green coloration of Co-doped ZnO explained from structural refinement and bond considerations, Inorg. Chem. 46 (2007) 10996–11002, https://doi.org/10.1021/ic701157j.
[40] D.K. Dubey, D.N. Singh, S. Kumar, C. Nayak, P. Kumbhakar, S.N. Jha, D. Bhattacharya, A.K. Ghosh, S. Chatterjee, Local structure and photocatalytic properties of sol–gel derived Mn–Li co-doped ZnO diluted magnetic semiconductor nanocrystals, RSC Adv. 6 (2016) 22852–22867, https://doi.org/10.1039/C5RA23220A.
[41] S. Ram, T.K. Mandal, Synthesis and characterization of thin ferroelectric PbZr0.52Ti0.48O3 fibrils, J. Am. Ceram. Soc. 88 (2005) 3444–3448, https://doi.org/10.1111/j.1551-2916.2005.00638.x.
[42] R.N. Das, Nanocrystalline ceramics from sucrose process, Mater. Lett. 47 (2001) 344–350, https://doi.org/10.1016/S0167-577X(00)00264-0.
[43] M. Ghaffari-Moghaddam, H. Eslahi, Synthesis, characterization and antibacterial properties of a novel nanocomposite based on polyaniline/polyvinyl alcohol/Ag, Arab. J. Chem. 7 (2014) 846–855, https://doi.org/10.1016/j.arabjc.2013.11.011.
[44] M.L. da Silva-Neto, M.C.A. de Oliveira, C.T. Dominguez, R.E.M. Lins, N. Rakov, C. B. de Araújo, L. de S. Menezes, H.P. de Oliveira, A.S.L. Gomes, UV random laser emission from flexible ZnO-Ag-enriched electrospun cellulose acetate fiber matrix, Sci. Rep. 9 (2019) 1–9, https://doi.org/10.1038/s41598-019-48056-w.
[45] M.N. Siddique, T. Ali, A. Ahmed, P. Tripathi, Enhanced electrical and thermal properties of pure and Ni substituted ZnO nanoparticles, Nano-Struct. Nano-Objects 16 (2018) 156–166, https://doi.org/10.1016/j.nanoso.2018.06.001.
[46] M. Arshad, A. Azam, A.S. Ahmed, S. Mollah, A.H. Naqvi, Effect of Co substitution on the structural and optical properties of ZnO nanoparticles synthesized by sol-gel route, J. Alloys Compd. 509 (2011) 8378–8381, https://doi.org/10.1016/j.jallcom.2011.05.047.
[47] R. Esparza, A. Santoveña, A. Ruíz-Baltazar, A. Angeles-Pascual, D. Bahena, J. Maya-Cornejo, J. Ledesma-García, R. Pérez, Study of PtPd bimetallic nanoparticles for fuel cell applications, Mater. Res. 20 (2017) 1193–1200, https://doi.org/10.1590/1980-5373-MR-2016-0934.
[48] K.S.W. Sing, D.H. Everett, R.A. Pierotti, J. Rouquerol, T. Siemieniewska, Reporting physisortion data for gas/solid systems with special reference to the determination of surface area and porosity, Pure Appl. Chem. 57 (1985) 603–619, https://doi.org/10.1351/pac198557040603.
[49] F. Yakuphanoglu, Electrical characterization and device characterization of ZnO microring shaped films by sol-gel method, J. Alloys Compd. 507 (2010) 184–189, https://doi.org/10.1016/j.jallcom.2010.07.151.
[50] S. Suwanboon, P. Amornpitoksuk, A. Haidoux, J.C. Tedenac, Structural and optical properties of undoped and aluminium doped zinc oxide nanoparticles via precipitation method at low temperature, J. Alloys Compd. 462 (2008) 335–339, https://doi.org/10.1016/j.jallcom.2007.08.048.
[51] A. Samanta, M.N. Goswami, P.K. Mahapatra, Influence of Nd3+ doping in ZnO nanoparticles to enhance the optical and photocatalytic activity, Mater. Res. Express 6 (2019), 65031, https://doi.org/10.1088/2053-1591/ab0c25.
[52] A. El Fakir, M. Sekkati, G. Schmerber, A. Belayachi, Z. Edfouf, M. Regragui, F. Cherkaoui El Moursli, Z. Sekkat, A. Dinia, A. Slaoui, M. Abd-Lefdil, Influence of rare earth (Nd and Tb) Co-doping on ZnO thin films properties, Phys. Status Solidi Curr. Top. Solid State Phys. 14 (2017) 2–5, https://doi.org/10.1002/pssc.201700169.

[53] R. Veerasubam, S. Muthukumaran, Role of defects in optical, photoluminescence and magnetic properties of Zn0.96−xNi0.04CrxO nanoparticles, J. Alloys Compd. 803 (2019) 240–249, https://doi.org/10.1016/j.jallcom.2019.06.299.
[54] N.M. Ravindra, S. Auluck, V.K. Srivastava, On the Penn gap in semiconductors, Phys. Status Solidi 93 (1979) K155–K160, https://doi.org/10.1002/pssb.2220930257.
[55] P. Hervé, L.K.J. Vandamme, General relation between refractive index and energy gap in semiconductors, Infrared Phys. Technol. 35 (1994) 609–615, https://doi.org/10.1016/1350-4495(94)90026-4.
[56] R.R. Reddy, S. Anjaneyulu, Analysis of the Moss and Ravindra relations, Phys. Status Solidi 174 (1992) K91–K93, https://doi.org/10.1002/pssb.2221740238.
[57] F. Naccarato, F. Ricci, J. Suntivich, G. Hautier, L. Wirtz, G.M. Rignanese, Searching for materials with high refractive index and wide band gap: a first-principles high-throughput study, Phys. Rev. Mater. 3 (2019) 1–13, https://doi.org/10.1103/PhysRevMaterials.3.044602.
[58] J. Muñoz-Flores, A. Herrera-Gomez, Resolving overlapping peaks in ARXPS data: the effect of noise and fitting method, J. Electron Spectros. Relat. Phenomena 184 (2012) 533–541, https://doi.org/10.1016/j.elspec.2011.08.004.
[59] D. Cabrera-German, G. Molar-Velázquez, G. Gómez-Sosa, W. de la Cruz, A. Herrera-Gomez, Detailed peak fitting analysis of the Zn 2p photoemission spectrum for metallic films and its initial oxidation stages, Surf. Interface Anal. 49 (2017) 1078–1087, https://doi.org/10.1002/sia.6280.
[60] A.J. Signorelli, R.G. Hayes, X-ray photoelectron spectroscopy of various core levels of lanthanide ions: the roles of monopole excitation and electrostatic coupling, Phys. Rev. B 8 (1973) 81–86, https://doi.org/10.1103/PhysRevB.8.81.
[61] S.B.M. Hagström, P.O. Hedén, H. Löfgren, Electron density of states in Yb metal as observed by X-ray photoemission, Solid State Commun. 8 (1970) 1245–1248, https://doi.org/10.1016/0038-1098(70)90369-8.
[62] K. Ugendar, S. Samanta, S. Rayaprol, V. Siruguri, G. Markandeyulu, B.R.K. Nanda, Effect of frustrated exchange interactions and spin-half-impurity on the electronic structure of strongly correlated NiFe2O4, Phys. Rev. B 96 (2017), 35138, https://doi.org/10.1103/PhysRevB.96.035138.
[63] C. Selvaraju, R. Karthick, R. Veerasubam, The modification of structural, optical and antibacterial activity properties of rare earth gadolinium-doped ZnO nanoparticles prepared by co-precipitation method, J. Inorg. Organomet. Polym. Mater. 29 (2019) 776–782, https://doi.org/10.1007/s10904-018-1051-0.
[64] K. Qi, B. Cheng, J. Yu, W. Ho, Review on the improvement of the photocatalytic and antibacterial activities of ZnO, J. Alloys Compd. 727 (2017) 792–820, https://doi.org/10.1016/j.jallcom.2017.08.142.
[65] S.S. Gill, N. Tuteja, Reactive oxygen species and antioxidant machinery in abiotic stress tolerance in crop plants, Plant Physiol. Biochem. 48 (2010) 909–930, https://doi.org/10.1016/j.plaphy.2010.08.016.
[66] A.S.H. Hameed, C. Karthikeyan, A.P. Ahamed, N. Thajuddin, N.S. Alharbi, S. A. Alharbi, G. Ravi, In vitro antibacterial activity of ZnO and Nd doped ZnO nanoparticles against ESBL producing Escherichia coli and Klebsiella pneumoniae, Sci. Rep. 6 (2016) 1–11, https://doi.org/10.1038/srep24312.
[67] C. Ayala-Castro, A. Saini, F.W. Outten, Fe-S cluster assembly pathways in bacteria, Microbiol. Mol. Biol. Rev. 72 (2008) 110–125, https://doi.org/10.1128/MMBR.00034-07.
[68] L. Zheng, V.L. Cash, D.H. Flint, D.R. Dean, Assembly of iron-sulfur clusters. Identification of an iscSUA-hscBA-fdx gene cluster from Azotobacter vinelandii, J. Biol. Chem. 273 (1998) 13264–13272, https://doi.org/10.1074/jbc.273.21.13264.
[69] P. Yuvaniyama, J. Agar, V. Cash, M. Johnson, D. Dean, NifS-directed assembly of a transient [2Fe-2S] cluster with the NifU protein, Proc. Natl. Acad. Sci. 97 (2000) 599–604, https://doi.org/10.1073/pnas.97.2.599.
[70] A.A. Mashruwala, Y.Y. Pang, Z. Rosario-Cruz, H.K. Chahal, M.A. Benson, L.A. Mike, E.P. Skaar, V.J. Torres, W.M. Nauseef, J.M. Boyd, Nfu facilitates the maturation of iron-sulfur proteins and participates in virulence in Staphylococcus aureus, Mol. Microbiol. 95 (2015) 383–409, https://doi.org/10.1111/mmi.12860.
[71] J.S. McQuillan, A.M. Shaw, Differential gene regulation in the Ag nanoparticle and Ag+-induced silver stress response in Escherichia coli: a full transcriptomic profile, Nanotoxicology. 8 (2014) 177–184, https://doi.org/10.3109/17435390.2013.870243.
[72] L. Palanikumar, S.N. Ramasamy, C. Balachandran, Size-dependent antimicrobial response of zinc oxide nanoparticles, IET Nanobiotechnol. 8 (2014) 111–117, https://doi.org/10.1049/iet-nbt.2012.0008.
[73] B. Zhang, L. Cui, K. Zhang, Dosage- and time-dependent antibacterial effect of zinc oxide nanoparticles determined by a highly uniform SERS negating undesired spectral variation, Anal. Bioanal. Chem. 408 (2016) 3853–3865, https://doi.org/10.1007/s00216-016-9478-z.
[74] G.N. Rajivgandhi, G. Ramachandran, N.S. Alharbi, S. Kadaikunnan, J.M. Khaleed, N. Manokaran, W.J. Li, Substantial effect of Cr doping on the antimicrobial activity of ZnO nanoparticles prepared by ultrasonication process, Mater. Sci. Eng. B Solid State Mater. Adv. Technol. 263 (2021), 114817, https://doi.org/10.1016/j.mseb.2020.114817.
[75] S. Angra, S. Ahuja, N. Emanet, H.R. Öz, N. Bayram, D. Delen, B. Nithya, V. Ilango, J. Schmidt, M.R.G.M.A.L. Marques, S. Botti, M.R.G.M.A.L. Marques, E.D. Kolaczyk, A.L. Oliveira, Predictive analytics in health care using machine learning tools and techniques, Int. Conf. Big Data Anal. Comput. Intell. 1 (2017) 57–60, https://doi.org/10.1109/ICBDACI.2017.8070809 (2017).
[76] N. Emanet, H.R. Öz, N. Bayram, D. Delen, A comparative analysis of machine learning methods for classification type decision problems in healthcare, Decis. Anal. 1 (2014) 1–20, https://doi.org/10.1186/2193-8636-1-6.
[77] J. Schmidt, M.R.G. Marques, S. Botti, M.A.L. Marques, Recent advances and applications of machine learning in solid-state materials science, Npj Comput. Mater. 5 (2019), https://doi.org/10.1038/s41524-019-0221-0.
[78] A.L. Oliveira, Biotechnology, big data and artificial intelligence, Biotechnol. J. 14 (2019) 1–6, https://doi.org/10.1002/biot.201800613.
[79] J. Demšar, T. Curk, A. Erjavec, Č. Gorup, T. Hočevar, M. Milutinovič, M. Možina, M. Polajnar, M. Toplak, A. Starič, M. Štajdohar, L. Umek, L. Žagar, J. Žbontar, M. Žitnik, B. Zupan, Orange: data mining toolbox in python, J. Mach. Learn. Res. 14 (2013) 2349–2353.